Journal of Hydrology 563 (2018) 303–318

Contents lists available at ScienceDirect

Journal of Hydrology

journal homepage: www.elsevier.com/locate/jhydrol

Research papers

Assessing the contribution of porewater discharge in carbon export and CO_2 evasion in a mangrove tidal creek (Can Gio, Vietnam)

Pierre Taillardat[a,*], Pim Willemsen[b,c,d], Cyril Marchand[e,f], Daniel A. Friess[a], David Widory[g], Paul Baudron[g,h], Van Vinh Truong[i], Thanh-Nho Nguyễn[e], Alan D. Ziegler[a]

[a] Department of Geography, National University of Singapore, 1 Arts Link, 117570, Singapore
[b] Water Engineering and Management, University of Twente, P.O. Box 217, 7500 AE Enschede, The Netherlands
[c] Deltares, Marine and Coastal Systems, Rotterdamseweg 185, P.O. Box 177, 2600 MH Delft, The Netherlands
[d] NIOZ Royal Netherlands Institute for Sea Research, Department of Estuarine and Delta Systems, and Utrecht University, P.O. Box 140, 4400 AC Yerseke, The Netherlands
[e] Department of Analytical Chemistry, University of Science, Vietnam National University, Ho Chi Minh City, 227 Nguyen Van Cu, Ho Chi Minh City, Viet Nam
[f] Institut de Recherche pour le Développement (IRD), UR 206/UMR 7590 IMPMC, 98848 Nouméa, New Caledonia, France
[g] Geotop – Department of Earth Sciences, Université du Québec à Montréal, Montréal, Canada
[h] Department of Civil, Geological and Mining Engineering, École Polytechnique de Montréal, C.P. 6079 Succ. Centre-Ville, Montréal, Québec H3C 3A7, Canada
[i] Department of Forest Resources Management, Nong Lam University, HCMC, Linh Trung, Thu Duc, Ho Chi Minh City, Viet Nam

ARTICLE INFO

This manuscript was handled by Fereidoun Rezanezhad, Editor-in-Chief, with the assistance of Fereidoun Rezanezhad, Associate Editor

Keywords:
Permeable sediments
Porewater discharge
Carbon cycling
Tidal exchange
Radon mass balance model

ABSTRACT

Although mangrove forests are efficient natural carbon sinks, most of the atmospheric carbon dioxide (CO_2) fixed by its vegetation is believed to be exported via tidal exchange, rather than stored in the vegetative biomass and sediment. However, the magnitude of tidal export is largely unknown because direct measurements are scarce. We deployed a novel experimental design that combined automated high-resolution measurements of hydrodynamic, hydrogeochemical and biogeochemical parameters during the dry season in a mangrove tidal creek in the Can Gio Mangrove Forest in Vietnam. The objective was to quantify the tide-controlled water, porewater, DIC and DOC exchange, and estimate the CO_2 evasion throughout tidal cycles contrasted by amplitude. Data from three 25-h time series showed a clear peak of DIC, DOC, pCO_2, and ^{222}Rn at low tide, particularly during tidal cycles of large amplitude, which directly relate to porewater discharge. Our mass balance models revealed that the tidal creek was a net exporter of dissolved carbon to coastal waters, with an important contribution (38%) coming from DIC in porewater discharge. Porewater exchange varied from 3.1 ± 1.6 to 7.1 ± 2.4 cm day^{-1}. DIC exchange ranged from 352 ± 34 to 678 ± 79 mmolC m^{-2} day^{-1}; DOC exchange, 20.6 ± 1.9 to 67.7 ± 7.9 mmol C m^{-2} day^{-1}; and CO_2 evasion, 69.9 ± 10.5 to 173.7 ± 26.1 mmolC m^{-2} day^{-1}. These estimates were in the high range of previous carbon assessments and were explained by (i) the monitoring station being located at equal distance from the head and the mouth of the creek, which minimized carbon degradation and losses associated to transport in water; and (ii) the site being a highly productive mangrove within South East Asia.

1. Introduction

Advances in mangrove ecology and biogeochemistry have been driven by the construction of two antagonistic paradigms. On the one hand, the outwelling hypothesis suggests that coastal wetlands export organic matter and nutrients to the offshore environment (Nixon, 1980; Odum, 1968; Odum, 2002), making mangroves play an important role supporting adjacent ecosystems and fisheries. Alternatively, the mangrove carbon sink concept suggests that mangroves are capable of storing large quantities of carbon per surface area, because of their high rates of primary productivity, sediment accretion, and carbon burial (Alongi, 2014). This source-versus-sink dichotomy illustrates the difficulty of identifying the direction of various ecological processes in dynamic tidal environments.

Global reviews on geomorphological contexts, hydrological settings, ecological behavior and biogeochemical dynamics have facilitated our understanding of mangrove environments and source-sink relationships. Based on geomorphological characteristics, mangroves are commonly described as a landform continuum subdivided into three general types with different ecological functions (Twilley and Rivera-Monroy,

* Corresponding author.
E-mail address: taillardat.pierre@u.nus.edu (P. Taillardat).

https://doi.org/10.1016/j.jhydrol.2018.05.042
Received 18 January 2018; Received in revised form 18 April 2018; Accepted 17 May 2018
Available online 29 May 2018

2009). Firstly, interior mangroves are only flooded a few days per month during spring tides and therefore are a net sink of carbon and nutrients derived from the mangrove vegetation. Secondly, fringe and riverine mangroves have the potential for intense outwelling that is controlled by strong river discharge to the coast. Thirdly, tide-dominated mangroves, which are the most common, are the most complex regarding outwelling and inwelling because of their daily bi-directional water tidal flows (Woodroffe, 1992).

The tide-dominated area of a mangrove forest contains a developed system of intricate tidal creeks of different lengths and sinuosity (Wolanski et al., 1980). In a typical tidal creek, no direct freshwater input from upstream rivers/streams occurs. At a daily time scale, water outflow, evapotranspiration and intertidal storage account for losses in the water budget (Michot et al., 2011; Nuttle and Harvey, 1995; Speer et al., 1991). Mutual feedback processes between hydrodynamics and geomorphology define the natural system of tidal creeks. Due to the complex hydrodynamics, it cannot be assumed the system is in equilibrium, only as highly stable (Wolanski et al., 1993).

Water (re)circulation is a key variable in tidal creeks, controlling most of the biogeochemical processes and their ecological implications (Fagherazzi et al., 2013; Wolanski et al., 1993). Although the mangrove outwelling theory has motivated substantial research, the nutritional significance and spatial extent of mangrove-derived organic matter is likely overestimated (Lee, 1995; Sousa and Dangremond, 2011). Conversely, the carbon storage sequestration potential of mangroves is gaining increased recognition because of the firmly established ability they have in trapping carbon (Alongi, 2014; Bouillon et al., 2008). Related in driving interest in carbon sequestration by mangroves is the need for countries having ratified the Paris Agreement to “achieve a balance between anthropogenic emissions by sources and removals by sink by 2100” (UNFCCC, 2015). Although the contribution of mangrove carbon sequestration at the global scale is probably limited because of the small total area they cover, it could be significant for countries with extensive mangrove coastlines.

Moreover, the fate of > 50% of carbon fixed by mangrove vegetation was until recently not clearly identified (Bouillon et al., 2008). Most of this missing carbon sink is now assumed to be transferred from mangrove forests to the coastal ocean via porewater discharge (from the mangrove sediment to the tidal creek) and tidal exchange (from the tidal creek to the coastal ocean) in the form of dissolved organic carbon (DOC) and, more importantly, dissolved inorganic carbon ($DIC = H_2CO_3 + HCO_3^- + CO_3^{2-} + CO_2$) (Alongi, 2014; Bouillon et al., 2007; Maher et al., 2013). If the tidal dissolved carbon export was validated globally, both the mangrove carbon sequestration potential and their ability to buffer high CO_2 atmospheric concentration could be higher than previously believed. However, a fraction of this DIC is in dissolved CO_2 form, which can potentially be re-emitted to the atmosphere (Abril et al., 2009; Atkins et al., 2013; Borges et al., 2003; Call et al., 2015; Linto et al., 2014). Similarly, the POC and DOC transiting in the creek water may also be consumed by the microbial community or photodegraded, producing CO_2 emission (Bouillon et al., 2003; Kristensen and Suraswadi, 2002). Further, the fate of DIC, once exported to coastal waters, could enhance calcium carbonate production (and therefore generate CO_2 emission), or remain in the water column as a net carbon sink (Macreadie et al., 2017; Smith, 2013). This inorganic outwelling would have only little relevance for the coastal food web, but large implications for the coastal carbon budget.

Only a few studies have directly quantified material fluxes in undisturbed mangrove tidal creeks, with a wide range of reported values and uncertainties (Bouillon et al., 2008). Furthermore, no study has quantified DIC exchange until recently (Maher et al., 2013; Sippo et al., 2016). The most commonly used approach is the Eulerian method, which integrates water discharge volume and element concentrations over different time periods (Twilley and Rivera-Monroy, 2009). Water exchange measurements are conducted through cross-section monitoring (Dittmar and Lara, 2001; Wattayakorn et al., 1990), flow-through flume experiments (Romigh et al., 2006; Twilley, 1985), hydrodynamic modelling (Ayukai et al., 1998; Boto and Wellington, 1988; Sánchez-Carrillo et al., 2009), or derived through remotely-sensed flooded area estimation (Boto and Bunt, 1981; Gleeson et al., 2013; Holloway et al., 2016; Sippo et al., 2016; Sippo et al., 2017; Tait et al., 2016; Twilley, 1985). Despite the extensive work the Eulerian approach requires, several studies mentioned the limited robustness of their results due to high variability and a near-balance exchange (Ayukai et al., 1998; Wattayakorn et al., 1990). Moreover, this method does not directly quantify the mangrove contribution, but only the water and material exchange in the tidal creek (Twilley and Rivera-Monroy, 2009). Among all the limitations, the inability to quantify water exchange accurately produces the most uncertainty. Current speed and water volume estimation are spatiotemporally heterogeneous and labor intensive to obtain. However, they are key variables requiring extremely precise measurements (Dittmar et al., 2009).

The quantification of a long-term hydrodynamic record can be achieved using high-definition quasi-continuous measurements from acoustic doppler instrument technology (Horstman et al., 2011; Kearney et al., 2017). Similarly, the use of automated *in situ* high-resolution instrumentation for partial pressure or carbon dioxide in water (pCO_2) and porewater/groundwater discharge (with the radioactive isotope radon (^{222}Rn) used as a proxy) enhance the accuracy and general understanding of the mangrove porewater contribution and carbon dynamics (Atkins et al., 2013; Call et al., 2015; Sadat-Noori et al., 2016, 2015).

In this study we investigate the role of a mangrove tidal creek in outwelling (tidal export) by quantifying porewater discharge, surface water exchange and carbon exchange across five characteristically different tidal cycles. The objectives of this study are twofold: (1) characterize the DOC, DIC, pCO_2 and ^{222}Rn concentration oscillations over five tidal cycles of different tidal amplitude, with the hypothesis that water level controls the porewater discharge and therefore the carbon dynamics in the tidal creek; and (2) quantify the creek water, porewater, DOC, DIC tidal exchange and CO_2 evasion rate over five contrasting tidal cycles based on mass balance budgets, with the hypothesis that the majority of the dissolved carbon is exported under the DIC fraction, rather than DOC export or CO_2 evasion, as a result of porewater discharge.

2. Methods

2.1. Study site

This study was conducted in a mangrove tidal creek in Can Gio UNESCO Biosphere Reserve (10 30.339′N; 106 52.943′E), south Vietnam (Fig. 1). The creek is approximately 1,400 m long and has no upstream freshwater input. Can Gio Mangrove is a mature replanted mangrove forest that was partly destroyed during the Vietnam-USA War (1961–1971). It is predominantly covered by *Rhizophora apiculata* with *Avicennia alba* occuring at the edge of the forest, along tidal creeks (Dung et al., 2016). Additionally, *A. officinalis, A. marina, A. rumphiana*, and *Sonneratia alba* were found during our survey along the edge of the tidal creek. The tidal regime over the lunar month exhibits strong diurnal inequality (Conley, 2015), with tidal amplitudes oscillating from symmetric (spring semi-diurnal tide) to asymmetric (neap diurnal tide) over a full cycle (≈25-h); maximal tidal amplitude reaches 3.18 m (Fig. 2). The annual mean precipitation is about 1,600–2,250 mm, with ~64% of the precipitation falling during the wet season (World Bank, 2017). The dry season occurs from late October to early May and the wet season from early May until the end of October. The study was conducted at the end of the dry season, from April 26th to May 8th, 2017. The annual mean temperature ranges from 26.5 °C to 30 °C.

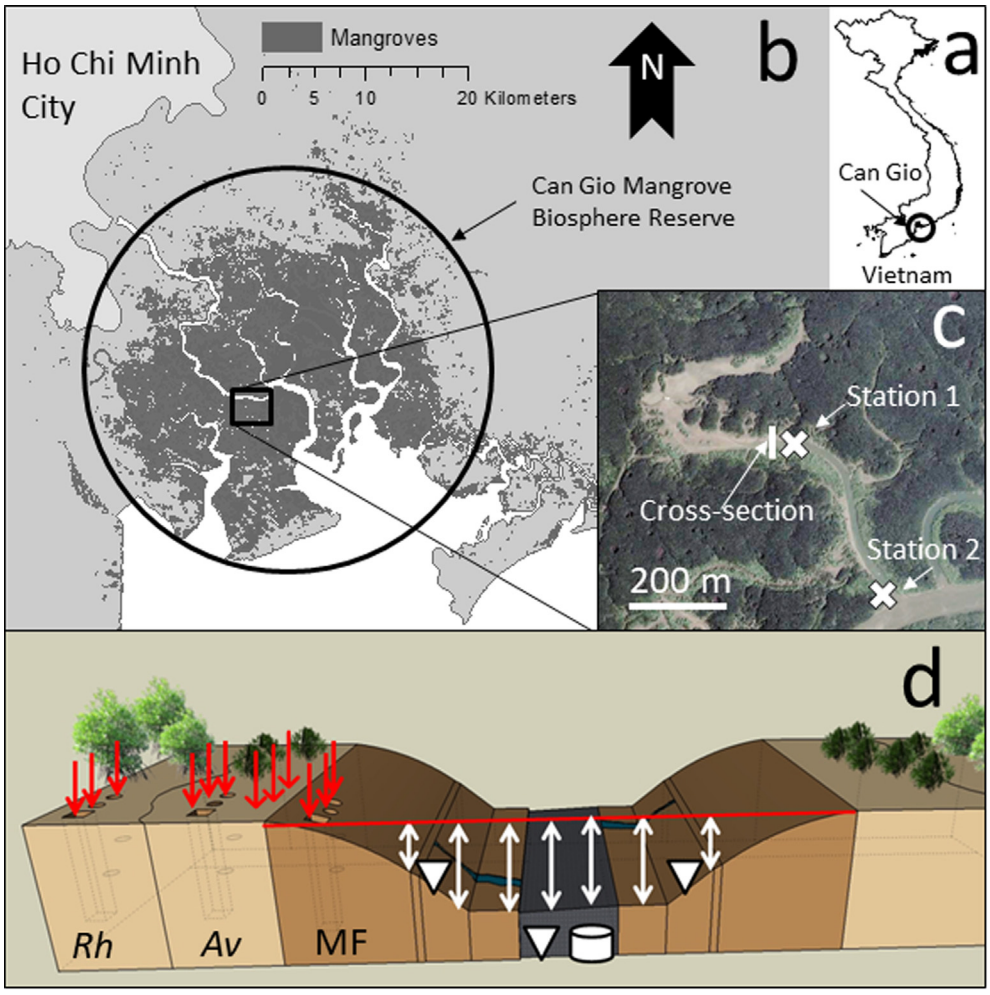

Fig. 1. (a) Map of Vietnam, with the black circle representing the location of study area; (b) Map of the Can Gio Mangrove UNESCO Biosphere Reserve study area located along the Saigon River, with the black square representing the study site; (c) Map of the mangrove tidal creek study site, with the white crosses representing the two locations where the 25-h time series sampling were conducted; (d) Conceptual model representing the cross-section set-up with the inverted triangles being the ADVs and the cylinder the ADCP. The cross-sectional vertical area was measured with Total Station measurements. The red arrows represent the triplicated porewater collection under the *Rhizophora (Rh)*, *Avicennia* (*Av*), a transition area at the top of the creek bank, and mudflat stands (MF). (For interpretation of the references to colour in this figure legend, the reader is referred to the web version of this article.)

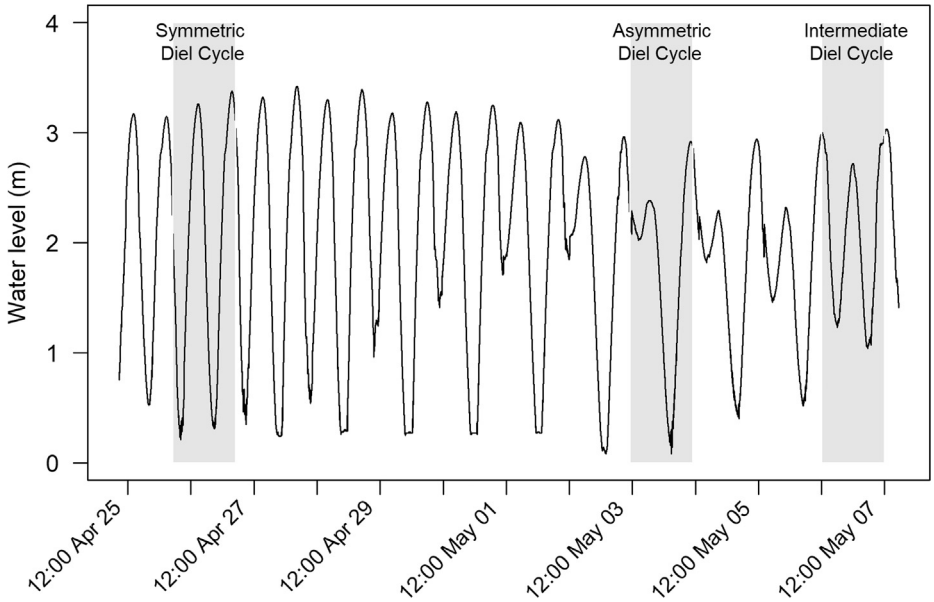

Fig. 2. Water level variation at the sampling station from April 25th to May 07th, 2017. Periods highlighted in grey are the three-time series presented in this study accounting for the symmetric, asymmetric and intermediate tidal cycles.

Table 1
Surface area (m^2) and maximum water volume (m^3) of the tidal creek catchment area.

	Upstream (Box A)	Downstream (Box B)	Total
Tidal Creek surface area (m^2)	36,356 (± 3,356)	28,234 (± 2,823)	64,590 (± 6,459)
Catchment surface area (m^2)	124,668 (± 24,934)	411,377 (± 82,275)	536,045 (± 107,209)
Max catchment flooded volume (m^3)	185,410 (± 55,623)	562,354 (± 168,706)	747,763 (± 224,329)

2.2. Experimental design and setup

A combination of automated high-frequency (minute time scale) equipment was deployed in a tidal creek and suspended from an anchored boat, which was used as the monitoring research station throughout 12 continuous days (Fig. 1). The sampling location (station 1) was chosen to have approximately equal creek surface area (m^2) upstream and downstream the monitoring station (Table 1). Three 25-h time series of data were collected over contrasting tidal cycles: (1) symmetric tidal cycle (04:30 am April 26th to 5:30 am April 27th, 2017); (2) asymmetric (11:30 am May 03rd 12:30 pm May 04th, 2017); and (3) intermediate (11:30 am May 06th to 12:30 pm May 07th, 2017). A complementary time-series was constructed at the creek mouth (station 2) during the study period (04:30 am April 28th to 5:30 pm April 28th, 2017) and is used in this study to predict ^{222}Rn input from the ocean during flood tide.

Flow velocity was determined using a combination of four types of measuring equipment placed along a cross-section (Fig. 1). The surface elevation (m) along the cross-section was measured using a Nikon Nivo 5 M Total Station to estimate cross-sectional vertical area (m^2) according to the water level height (m), which was determined from a water level logger located 5 m downstream. From the monitoring station, located 15 m downstream from the cross-section, temperature, dissolved oxygen (DO), wind speed, pCO_2, and ^{222}Rn were recorded continually at 1 sec to 30 min intervals, based on the different equipment reading period required. Discrete samples of surface water for DOC and total alkalinity (TAlk) were also collected every hour.

During each time-series, one to two periods of steady state water budget integrating one ebb and one flood tide were used for developing a mass balance model. In this study, we refer to the daily 25-h tidal cycle as the"diel cycle" and the selected water balanced period as the "tidal cycle".

Porewater samples were collected along one elevation gradient/ecotone transect (*Rhizophora*-dominated, *Avicennia*-dominated, and mudflat stand), from the mangrove forest to the tidal creek, to characterize the mangrove porewater end-member concentrations (Fig. 1d). All collected data were eventually combined to construct mass balance models based on the hydrodynamics, radioactive isotopes, and biogeochemical concentrations.

Although prior studies quantified tidal creek exchange from the mouth (Maher et al., 2013; Romigh et al., 2006; Sippo et al., 2016; Tait et al., 2016), we intentionally located our research station midway from the head and mouth of the tidal creek to obtain the most representative estimation of the tidal creek exchange. This central location has two advantages: (1) minimizes the influence of water intrusion and eddy flow in the tidal creek from the downstream channel which tends to affect the accuracy of water discharge estimates (Mazda et al., 2002); and (2) increases the accuracy of the gas evasion estimates as a clear gradient was described for CO_2 and ^{222}Rn evasion from upstream to downstream from previous studies (Call et al., 2015; Leopold et al., 2017).

2.3. Creek surface water measurements and analysis

From the monitoring station, creek water was pumped from a depth of ≈20 cm using a submersible pump into a showerhead gas-air equilibrator. This equilibrator chamber was connected to the following: (1) a Drierite desiccant chamber; (2) a pre-calibrated (0 ppm, 545 ppm, 2867 ppm) non-dispersive infra-red CO_2 gas analyzer (LiCor 820) for pCO_2 measurements (± 1 µatm, 1 measurement per sec); and (3) an automated ^{222}Rn-in-air analyzer with the Rad Aqua package installed (RAD7, Durridge) for radon (^{222}Rn) in water measurements (Baudron et al., 2015; Burnett et al., 2001; Santos et al., 2012b). The radon monitor logged data at 30 min intervals. As a common feature when using the radon in water package (Sadat-Noori et al., 2015), the radon analytical uncertainty was on average 24% but up to 65% during the low-concentration high tide values at the beginning of our time series, when the equilibration time for the equipment was not yet reached (the first 3-h only) (Burnett and Dulaiova, 2003). Water temperature and pH were recorded every five minutes using a YSI 6920 multi-parameter water-quality probe, calibrated before each time series for pH, with buffers of 4.0, 7.0 and 10.0. Dissolved oxygen was measured using a Hobo U26-001 dissolved oxygen data logger, calibrated before each time series at 100% and 0% oxygen saturation. A Kestrel 5400 Heat Stress Tracker was also deployed on top of the boat for air temperature and wind speed measurements every 5 min.

Discrete surface water samples were collected every hour during the 25-h time series using a bucket (≈20 cm depth). All samples were filtered using Sartorius® Minisart-plus cellulose acetate/glass-fibre syringe filters (0.45 µm) and stored in 50-mL PP tubes for total alkalinity (Talk) measurements and in 15-mL PP tubes with ~0.02 mL of suprapur H_3PO_4 (85%) to reduce pH below 2 for dissolved organic carbon (DOC). All the samples were kept in a cooler until returning to the laboratory. DOC was analyzed using an Elementar Vario TOC cube analyzer, employing the combustion catalytic oxidation method (Sugimura and Suzuki, 1988). Total Alkalinity was determined by Gran electrotitration (Gran, 1952). DIC was calculated from TAlk and pCO_2 using CO_2SYS (Lewis and Wallace, 1998), with the carbonate dissociation constants K_1 and K_2, based on values reported by (Mehrbach, 1973) and modified by Dickson and Millero (1987).

2.4. Mangrove porewater measurements

Porewater samples were collected along one elevation gradient/ecotone transect, extending from the mangrove forest towards the tidal creek (*Rhizophora*-dominated, *Avicennia*-dominated, and mudflat stand, Fig. 1). For each plot, three bore holes of ≈60 cm depth were excavated with a shovel. The water in each bore was purged three times before collection via a suction tube. Three piezometers of 50 cm, 100 cm, and 150 cm depths were installed at the mudflat/*Avicennia*-dominated ecotone with water sample collected via suction tube. Sampling of TAlk and DOC values were done as described for the creek water samples. A volume of 1.5 L per bore was analyzed within 6 h using the RAD7's Rad-H_2O Big Bottle system (Durridge) for ^{222}Rn measurements. Gas evasion was minimized when collecting water for ^{222}Rn measurements by placing the end of the tube in the bottom side of the bottle and releasing the water slowly to minimize bubbling and exchanges with air (Dulaiova et al., 2008). A correction for ^{222}Rn decay was applied, based on the time period between the collection and analysis for each sample. The choice of triplicate samples per plot was made to buffer the existing

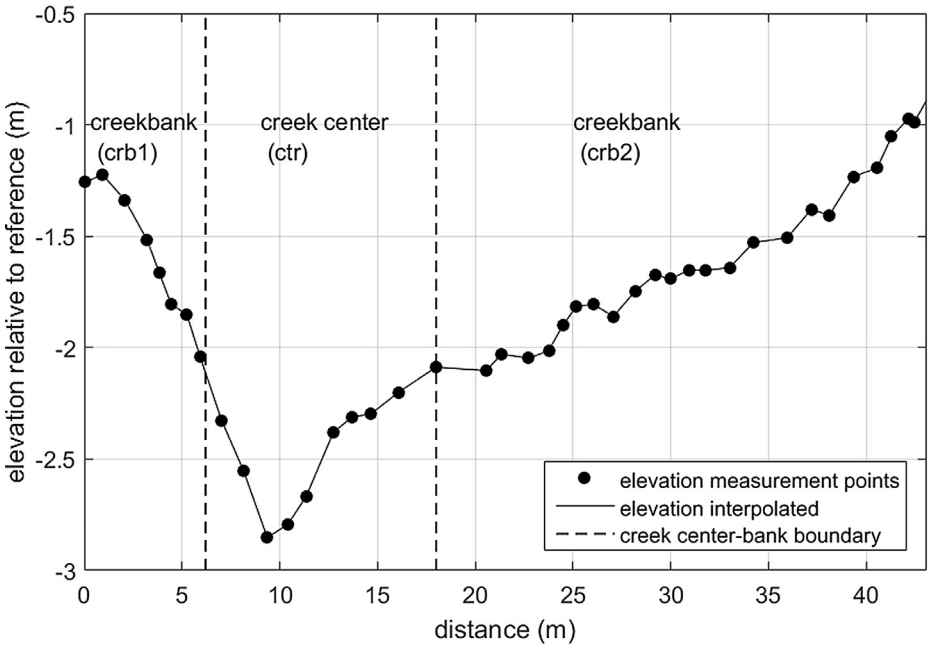

Fig. 3. Cross-section (SSE to NNE) located in the middle of the tidal creek and where the hydrodynamic measurements were operated. One ADV was installed at each of the three portions (crb1, ctr, and crb2) and the ADCP-HR at the lowest point of the ctr portion. The elevation measured was relative the Total Station level (reference).

sediment heterogeneity between and within mangrove land cover stands.

Triplicate soil cores of 100 cm depth were also taken at each plot. Sediment layers were sectioned at 5 cm intervals on the 100-cm sediment core until reaching 70 cm depth, after which measurements were taken every 10 cm until 100 cm depth. Grain size fraction were analyzed using a Mastersizer 2000 particle size analyser (Malvern Instruments). Organic carbon percentage (%OC) was determined using an elemental analyzer (NC instruments NC2500^{TM}) after drying, sieving, and fumigating (HCl 1 N) the soil samples (one core only per stand).

2.5. Hydrodynamics measurements and analysis

To obtain the exchange of water inward and outward from the creek, we first measured the cross-section. Coordinates and the relative depth of the cross-section were obtained via land surveying methods using a Nikon Nivo 5 M Total Station, with a horizontal and vertical accuracy of ± 6.25 mm. The Total Station was mounted on a tripod installed on the creek bank with a clear field of view of the entire creek, and a pole-mounted prism was moved across the creek to take spot elevation measurements. Measurements were taken approximately every 5 cm or where a clear break in elevation was observed (Fig. 3).

Flow velocities were obtained using three Nortek Acoustic Doppler Velocimeters (ADVs) and one Nortek Acoustic Doppler Current Profiler – High Resolution (ADCP-HR), placed along the cross-section, perpendicular to the tidal creek (Fig. 1). Two ADVs were placed at both creek banks, while the ADCP-HR and the third ADV were deployed in the center at the deepest part of the tidal creek, with the ADV located downstream from the ADCP-HR. Additionally, water levels were recorded every 1 min continuously over the full spring-neap cycle using a MX2001-01-Ti-S water level logger (Hobo Onset) installed at the center of the creek, approximately 5 m downstream from the cross-section. The coordinates and elevation of the water level probe location were also taken using the total station.

Flow velocities at a single point, in horizontal (x, y) and vertical (z) directions, were monitored using the ADVs. The ADV heads were mounted downward-looking, with the point measurement being 0.07 m above the bed, to maximize the measurement period during low tide. Flow velocities were collected when the water level exceeded approximately 0.25 m. The frame of the ADVs was oriented perpendicular to the prevailing flow velocities, which were driven by the tides, for reducing flow disturbances. The probe heads were aligned north. This set-up was similar to Willemsen et al. (2016). The sampling rate of the ADVs was 16 Hz, with 1024 samples (64 s) per burst and a burst interval of 180 s.

Vertical flow velocity profiles were mapped using the ADCP-HR, which was installed upward-looking, with the head 0.4 m above the bed. The blanking distance, which is the vertical area near the ADCP head where taking reasonable measurements was not possible, was 0.10 m. The profile range was 0.50 m, with a cell size of 20 mm. Therefore, measurements were obtained between 0.5 m and 1.0 m above the bed. The ADCP-HR was mounted using a frame with horizontal canes below the head and vertical canes, exceeding the height of the ADCP-HR, perpendicular to the prevailing flow direction. In addition to the flow velocity profile, water levels were recorded using the pressure sensor of the ADCP-HR. The sampling rate of the ADCP-HR depended on the duration of the measurement 2 Hz, with 120 samples (60 s) per burst and a burst interval of 120 s or of 300 s.

Hydrodynamic data (ADVs and ADCP-HR) were pre-processed and filtered. Noise in the ADV data-caused by neighboring animal activity, passing boats and air bubbles-was filtered by replacing samples with a mean correlation of the return signal below 70% with NaN (SonTek, 1997). Filtered data were burst-averaged to provide a continuous 25-h time series for the different measurement periods. Inaccurate ADCP-HR data were filtered using a noise floor of 150 counts, consequently removing all signals influenced by reflections at and above the water surface (Horstman et al., 2013).

2.6. Mass balance models and calculations

2.6.1. Hydrodynamic fluxes

Tidal creek water exchange (export towards the mouth during ebb tide and import towards the origin during flood tide) was estimated by multiplying flow velocity rates (m per 15 min) with the flooded vertical cross-section area (m^2) at a 15-min time frame to obtain a water discharge rate (m^3 per 15 min). Water exchange was further used for calculating dissolved carbon exchange and porewater exchange.

Depth-averaged flow velocities were calculated at three locations in the tidal creek (center, left bank and right bank). A relation between the depth-averaged velocity ($U_{d,ctr}$) and velocity at 0.07 m ($U_{0.07,ctr}$) from the bed (were the ADVs were installed; Fig. 1) was obtained using the

ADV and ADCP measurements at the center of the creek. The depth-averaged flow velocity was derived from the flow velocity profile composed from ADV and ADCP measurements and related to the flow velocity at 0.07 m from the bed. This approach resulted in a following linear relation (Eq. (1)), with a coefficient of determination (R^2) of 0.84 (not shown). The depth-averaged velocity at both creek banks ($U_{d,crb1}$ for left creek bank ; $U_{d,crb2}$ for right creek bank) was calculated by applying the linear relation (Eq. (1)), to the measurements (ADV) obtained at 0.07 m above the bed ($U_{0.07,crb1}$; $U_{0.07,crb2}$). By applying this method, three depth-averaged flow velocities were obtained ($U_{d,n}$,$n = ctr,crb1,crb2$): one for the center creek, one for the left creek bank and one for the right creek bank.

$$U_{d,n} = 3.9 \cdot 10^{-3} - 1.02 \cdot U_{0.07,n} \quad (1)$$

Cross-sectional vertical area (A) per 15 min time step was calculated by combining the relative elevation of the cross-section (Fig. 3) with water level measurements from the ADCP. The cross-section was distributed over three sub-sections similar to the hydrodynamic measurements, two creek banks and the creek center. Water exchange per sub-section was calculated by multiplying the depth-averaged velocity by the cross-sectional vertical area, per sub-section. Total water exchange (Q) was calculated by adding the water exchange through the creek center (Q_{ctr}), and over both creek banks (Q_{crb1}, Q_{crb2}).

2.6.2. Dissolved carbon mass balance model

Hydrodynamic and biogeochemical data were used to infer fluxes of carbon at hourly intervals throughout the 25-h time series using a Eulerian approach (Twilley and Rivera-Monroy, 2009):

$$DOC_{exchange} \text{ or } DIC_{exchange} = Q \cdot DOC_{cw} \text{ or } Q \cdot DIC_{cw} \quad (2)$$

where at each 60 min, Q is the water exchange ($m^3\ h^{-1}$); DOC_{cw} or DIC_{cw} are the measured surface water carbon concentration of DOC or DIC (mmol m^{-3}). The dissolved carbon flux (mmolC h^{-1}) was then integrated over the individual ebb and flood period, normalised their respective catchment area (mmolC m^{-2} tidal $cycle^{-1}$), and to a daily rate (mmolC m^{-2} day^{-1}).

2.6.3. Radon mass balance model

A radon mass balance model developed by Peterson et al. (2010) and modified by Sadat-Noori et al. (2015) was adapted, to estimate porewater discharge into the tidal creek over balanced tidal cycles. The use of the radon gas tracer for estimates of groundwater contribution lies in the principle that the budget residual from all the accounted radon sources (ingoing surface import, ^{226}Ra decay, ^{222}Rn molecular diffusion) and sinks (^{222}Rn decay, ^{222}Rn atmospheric evasion, and outgoing surface export) in a closed system is inherently attributable to sub-surface discharge. While Peterson et al. (2010) showed the relevance of continuous radon measurements for porewater seepage characterization, Sadat-Noori et al. (2016) enhanced this approach by conducting simultaneous and complementary measurements at different locations within the studied system. Following the same approach, we fragmented the studied tidal creek into two boxes. Box A being the area upstream the monitoring station 1 and assessed during the flood tide, and box B the downstream area assessed during the ebb tide. A conceptual model of the radon mass balance is presented in Fig. 4. The following equations were used in this study:

$$Ebb\ PW_{exchange} = \frac{(Rn_{st1} \cdot Q) + (RnJ_{atm} \cdot A_{creek}) + (Rn_{st1} \cdot \lambda_{Rn} \cdot \mathrm{VolA}_{cat}) - (Ra_{decay} \cdot \lambda_{Rn} \cdot \mathrm{VolA}_{cat}) - (Rn_{diff} \cdot A_{cat})}{Rn_{end\ member}} \quad (3)$$

where at each 30 min, Rn_{st1} is the mean ^{222}Rn concentration of the water column at the time series station (dpm m^{-3}); Q is the volume of water exchanged during the time period (m^3); RnJ_{atm} is the atmospheric evasion of ^{222}Rn due to wind, water velocity, water depth (dpm m^{-2}); A_{creek} is the creek upstream estimated flooded surface area (m^2); λ_{Rn} is the decay constant of ^{222}Rn per 30′ ($3.77\ 10^{-3}$); $VolA_{cat}$ is the estimated water volume in the upstream catchment area (i.e. Box A) (m^3); Ra_{decay} is the ^{222}Rn concentration produced through the decay of ^{226}Ra (dpm m^{-3}); Rn_{diff} is the diffusion of ^{222}Rn form sediments (dpm m^{-2}); A_{cat} is the is the upstream catchment (i.e. Box A creek and forest cover) estimated flooded surface area (m^2); $Rn_{end\ member}$ is the median ^{222}Rn concentration in the porewater bores (dpm m^{-3}) minus the median surface water ^{222}Rn concentration per diel cycle, to consider seawater recirculation.

A comparable equation with Eq. (3) was used during flood tide, with

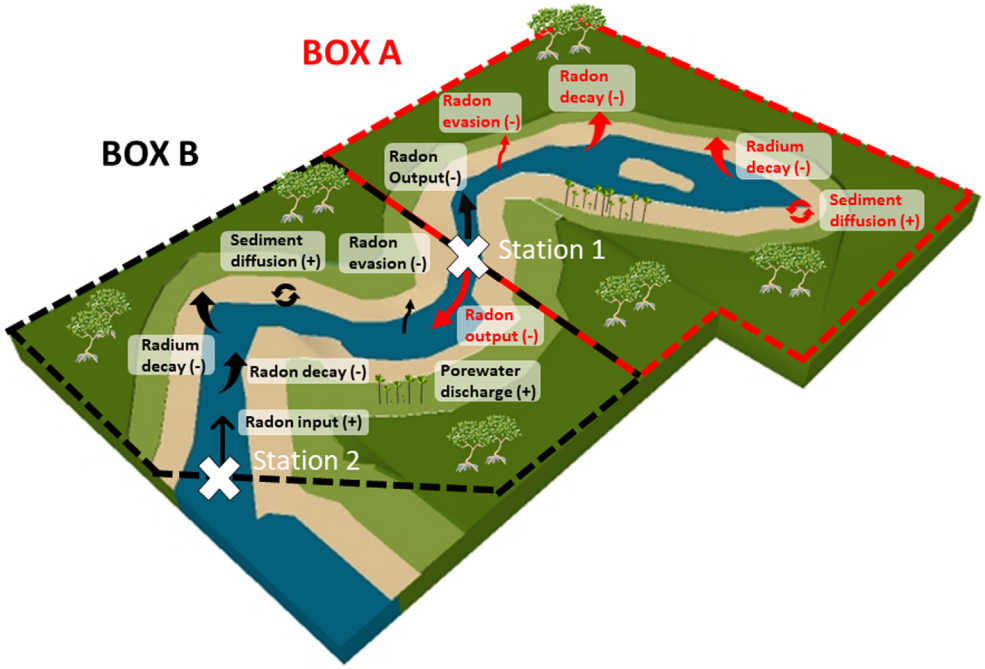

Fig. 4. Conceptual model of the radon mass balance budget. The tidal creek is separated in two components (box A and B). (+) indicates sources of carbon; (-) indicate sinks of carbon.

the difference that (i) the surface area was downstream the monitoring station (i.e. box B), and (ii) radon input from the ocean accounted for an additional source:

$$Flood\ PW_{exchange} = \frac{(Rn_{st1-st2}\cdot Q) + (RnJ_{atm}\cdot B_{creek}) + (Rn_{st1-st2}\cdot\lambda_{Rn}\cdot VolB_{cat}) - (Ra_{decay}\cdot\lambda_{Rn}\cdot VolB_{cat}) - (Rn_{diff}\cdot B_{cat})}{Rn_{end\ member}} \quad (4)$$

where at each 30 min, $Rn_{st1-st2}$ is the value difference between ^{222}Rn concentration of the water column at mid creek (station 1) and creek mouth (station 2) (dpm m^{-3}); B_{creek} is the creek downstream estimated flooded surface area (m^2); $VolB_{cat}$ is the estimated water volume of the downstream catchment area; B_{cat} is the is the downsttream catchment (i.e. creek and forest cover) estimated flooded surface area (m^2).

The creek (A_{creek}, B_{creek}) and catchment (A_{cat}, B_{cat}) surface area were estimated in Google Earth Pro. The flooded area and water volume in the catchment area were estimated by combining the surface area estimation, the cross-section topography extrapolated to the whole creek area, and the continuous water level measurements. The Ra_{decay} was measured via discrete sampling taken every two hours (n = 13) during the intermediate tidal cycle only. Water samples of 140 L were filtered through 20 g dry wet of manganese oxide-impregnated (MnO_2) acrylic fiber (Baudron et al. 2015). The fiber samples were analyzed for ^{226}Ra concentrations using the RaDeCC system (Radium Delayed Coincidence Counting). The Rn_{diff} was determined by incubating 1.5 L of sediment with 4.5 L of radon-free water in a sealed glass bottle for two months to reach the ^{222}Rn equilibrium stage (Baudron et al., 2015; Gleeson et al., 2013; Santos et al., 2012a). The overlying water from the incubation experiment was then analyzed using the RAD7 Rad-H_2O Big Bottle system for ^{222}Rn measurements. The Rn_{diff} was then calculated as described in (Martens et al., 1980):

$$Rn_{diff} = \sqrt{\lambda D_s}\,(C_{eq} - C_{cw}) \quad (5)$$

where λ is the radon decay constant (0.181 day^{-1}); D_s is the effective radon diffusion coefficient in sediments (m^2 day^{-1}); C_{eq} is the measured value from equilibration experiment activity in porewater (dpm m^{-3}); and C_{cw} is the measured value from surface creek water (dpm m^{-3}). The D_s was calculated as presented by Ullman and Aller (1982) and Peng et al. (1974).

$$D_s = \varnothing\left(10^{\left[-\left(\frac{980}{T}\right)+1.59\right]}\right) \quad (6)$$

where $\varnothing$ is a ratio that reflects the fraction of total ion exchangeable of ^{222}Rn under the dissolved form in porewater and estimated to be equal to 1 in mangrove sediments (Stieglitz et al., 2013); and T is water temperature (K).

During the ebb tide, the mass balance integrated measurements for the upstream area (box A). During the flood tide, the mass balance integrated measurements for the downstream area (box B), including radon input from downstream the creek mouth (station 2). Because of logistical restrictions, we could not conduct simultaneous measurements at station 1 and station 2. Thus, the downstream radon input in our mass balance budget was predicted using the water level as a reference as we found a strong relationship between water level and radon at both, station 1 and station 2 during our survey using an exponential equation (Fig. 5).

Values in m^3 tidal cycle^{-1} were converted into cm tidal cycle^{-1} by integrating the porewater discharge rate to the maximum flooded individual catchment surface area (m^2) to consider the surface area variability between box A and box B. $Flood\ PW_{exchange}$ and $Ebb\ PW_{exchange}$.were then summed, divided by the duration of the steady state tidal cycle, and multiplied by 24-h (i.e. cm day^{-1}) to provide a daily rate. Uncertainties of the radon mass balance model were reported using the error propagation approach.

The contribution of porewater discharge over the total water volume was then estimated from Eq. (3) and Eq.1 ($PW_{exchange}/Creek\ water_{exchange}$, in %). The contribution of porewater-derived DOC and DIC was determined using the porewater discharge volume for the radon mass balance (m^3 h^{-1} from Eq. (3) and multiplied by the median porewater DOC and DIC concentrations (mmol m^{-3}):

$$DOCPW_{exchange}\ or\ DICPW_{exchange} = PW_{exchange}\cdot DOC_{end\ member}\ or\ PW_{exchange}\cdot DIC_{end\ member} \quad (7)$$

Median values ± median absolute deviation are presented due to the non-normal distribution of the surface water and porewater concentrations. The contribution porewater-derived DOC or DIC exchange over the total DOC or DIC exchange was estimated from Eq. (7) and the normalized sum of Eq. (2) + Eq. (3) ($DOCPW_{exchange}/DOC_{exchange}$ or $DICPW_{exchange}/DIC_{exchange}$).

2.6.4. Atmospheric ^{222}Rn and CO_2 evasion

Both ^{222}Rn and CO_2 are subject to outgassing from the water column toward the atmosphere because of concentration gradient differences and water turbidity transfer (Borges and Abril, 2011; Wanninkhof et al., 2009). The gas atmospheric evasion flux (J_{atm}) was estimated as follow:

$$J_{atm} = k \propto (Cw - Cair) \quad (8)$$

where k is the gas-transfer velocity at the water-atmosphere interface (m h^{-1}); Cw and $Cair$ are the gas concentrations in water and air

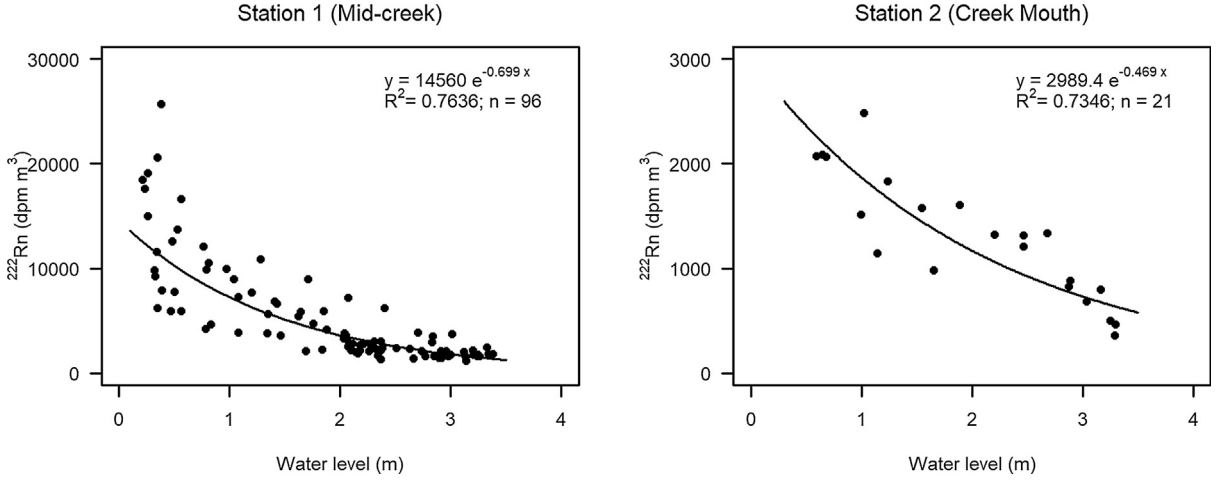

Fig. 5. Correlation between water level and radon concentrations at station 1 (mid-creek) and station 2 (mouth). The correlation at station 2 is used for predicting the radon concentrations input for the box B radon mass balance model.

(µatm); and α is the solubility coefficient (mmol m^{-3} atm^{-1}) expressed as a function of temperature and salinity (Wanninkhof et al., 2009; Weiss, 1974). The gas transfer velocity *k*, was normalized to the Schmidt number of 600 (Wanninkhof, 1992; Wanninkhof, 2014; Wanninkhof et al., 2009).

We selected four theoretical gas transfer velocity models (*k*) which were developed or previously used in mangrove creek environments that integrate both (1) water level (2) wind speed normalized at 10 m (U_{10}; obtained using Amorocho and DeVries (1980) and (3) current velocity. The mean of the four calculated gas transfer velocities was used to determine the atmospheric evasion flux (FCO_2). The first equation is as follows (Borges et al., 2003):

$$k = (1 + 1.719v^{0.5}h^{-0.5} + 2.58U_{10})(Sc/600)^n \quad (9)$$

where *v* is the current velocity (cm s^{-1}); *h* the water depth (m); U_{10} the wind speed (m s^{-1}); *Sc* the Schmidt number determined using the coefficients from Wanninkhof (2014) and the temperature variation measured during the field survey; and n is the Schmidt exponent, which we set to-0.5 in highly turbulent environments (Abril et al., 2009). The second (Ho et al., 2014), third (Ho et al., 2016) and fourth equations (Rosentreter et al. 2016) are as follow:

$$k = (1.58e^{0.3U\,10} + 1.529v^{0.5}h^{-0.5})(Sc/600)^n \quad (10)$$

$$k = 0.77\,v^{0.5}h^{-0.5} + 0.266\,U_{10}^2\,(Sc/600)^n \quad (11)$$

$$k = (-0.08 + 0.26v + 0.83\,U_{10} + 0.59\,h)(Sc/600)^n \quad (12)$$

where k, v, U_{10} h, Sc, and n are as above. From these equations, tidal creek outgassing rates were calculated at 5 min intervals and integrated over the 25-h times series periods.

3. Results

3.1. Biogeochemistry

3.1.1. Surface water observations

Dissolved organic carbon (DOC), dissolved inorganic carbon (DIC), the CO_2 partial pressure (pCO_2) and radon (^{222}Rn) in the creek water surface followed a tidal trend throughout the diel cycles, with higher concentrations during the low tide periods (Fig. 6). Concentration ranges over the three diel cycles were all within the same order of magnitude for each variable. DIC concentrations ranged from 1,085 to 2,699 mmol m^{-3} while DOC concentrations only oscillated from 78 to 165 mmol m^{-3}, which is about an order of magnitude lower. The pCO_2 concentrations oscillated from 1,088 µatm to 17,767 µatm and the radon concentrations from 744 dpm m^{-3} to 25,680 dpm m^{-3} (Fig. 6).

Complementary to those overall homogeneous trends, three irregularities between tidal cycles were observed. First, DOC during and between tidal cycles had a distinct behavior when compared with the other variables. DOC concentrations were significantly lower (Kruskall-Wallis $H_{3,72} = 16.9$; $p < 0.001$) during the symmetric tidal cycle (median ± median absolute deviation = 104 ± 24 mmol m^{-3}), when compared with the asymmetric (127 ± 9 mmol m^{-3}) and intermediate

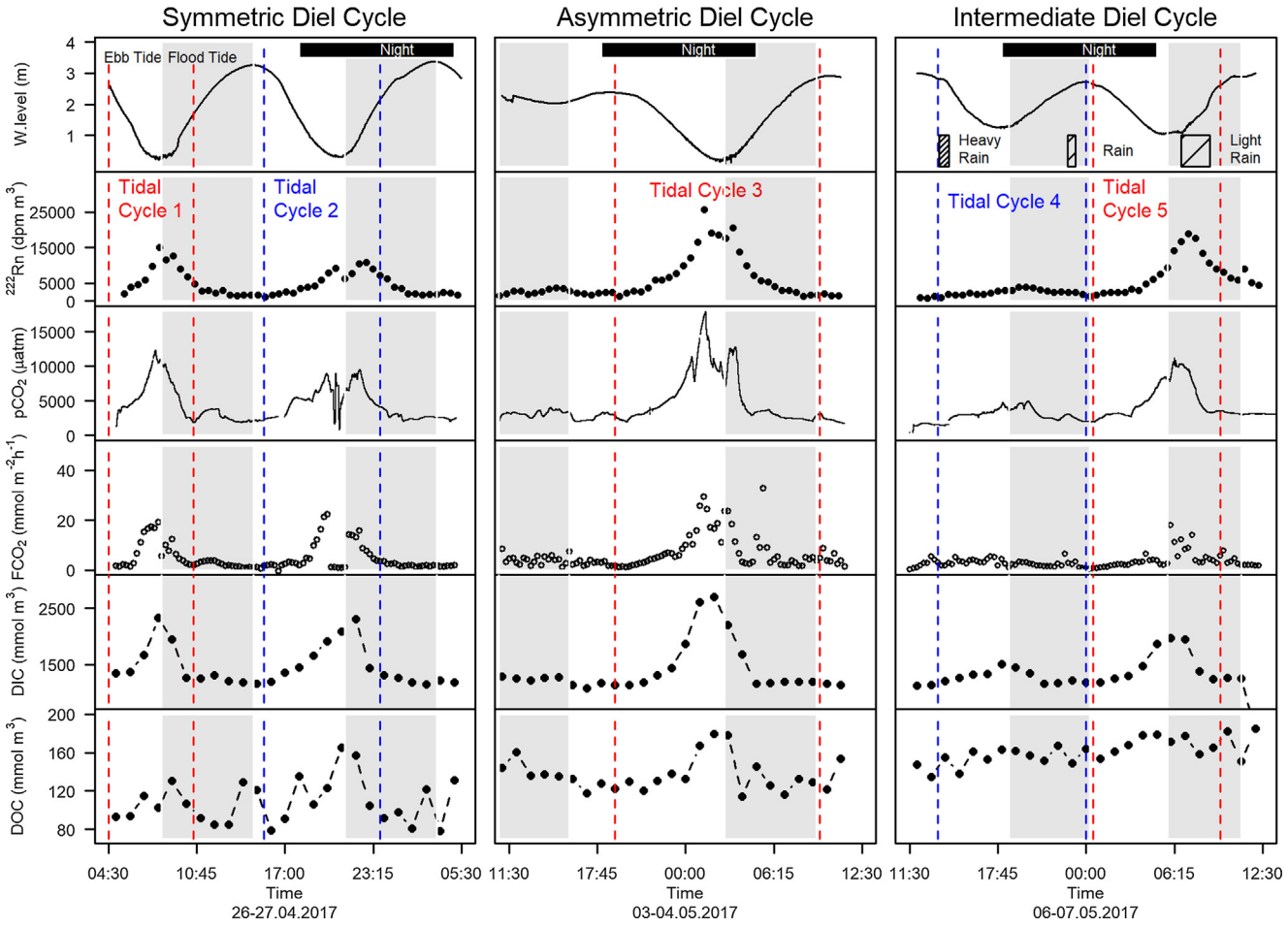

Fig. 6. Diel cycle (25-h) of water level, radon (^{222}Rn) and several carbon parameters in the Can Gio Mangrove tidal creek in April and May 2017 (Dry Season Symmetric, Asymmetric, and Intermediate tides). The grey background indicates flood tide; no background (white) indicates ebb tide; the black banner at the top indicates night.

Table 2
Porewater grain size fraction, ^{222}Rn (dpm m^{-3}), DIC (mmol m^{-3}) and DOC (mmol m^{-3}) concentrations. Median, standard deviation (STDEV) and standard error (SE) are presented. AV-MF stands for the Avicennia-dominated/Mudflat transition plot.

	Sand (%)	Silt (%)	Clay (%)	OC (%)	^{222}Rn (dpm m^{-3})	DIC (mmol m^{-3})	DOC (mmol m^{-3})
Rhizophora 1	9.4	82.7	7.8	6.7	91,687	2099	144
Rhizophora 2	20.9	72.6	6.6		33,796	2347	143
Rhizophora 3	14.5	78.1	7.4		35,682	1377	154
Avicennia 1	2.1	90.5	7.4	2.3	31,362	6240	204
Avicennia 2	1.8	89.5	8.7		57,434	4318	152
Avicennia 3	1.1	90.3	8.6		87,384	4861	401
Mudflat 1	3.6	87.8	8.5	2.4	117,715	8661	305
Mudflat 2	5.0	86.0	8.8		164,160	7014	284
Mudflat 3	8.6	88.8	2.5		103,456	6961	257
Av-MF 50 cm					25,360	NA	204
Av-MF 100 cm					69,040	NA	267
Av-MF 150 cm					88,326	NA	231
Median	**5.0**	**87.8**	**7.8**		**77,520**	**4,861**	**219**
STDEV	**6.7**	**6.2**	**2.0**		**41,660**	**2,398**	**78.6**
SE					**14,469**	**847.9**	**23.9**

(127 ± 6 mmol m^{-3}) tidal cycles. The tidal oscillations were also less pronounced for DOC, particularly during the intermediate diel cycle as no low-tide peak was detected (Fig. 6). Concentration changes between low and high tide were also of smaller magnitude for DOC, with differences of only 86.7 µM, 28.3 µM, and 18.7 µM for symmetric, asymmetric and intermediate tidal cycles, respectively.

The second irregularity, which was observed for the four variables assessed, was the absence of the concentration peak mentioned above during the first low tide of the asymmetric and intermediate diel cycle (Fig. 6). The peak absence occurred during high low tides. These time periods could be described as high low tide as the lowest water level during this period was 2.03 m and 1.24 m, respectively (Fig. 6). In comparison, the height of the creek bank at the sampling station is 1.94 m. Although the two low-tide periods of the symmetric diel cycle clearly showed increasing concentrations, the highest DIC, pCO_2, and radon concentrations at low tide occurred during the asymmetric tidal cycle 3 (Fig. 6).

The third irregularity was specific to the intermediate tidal cycle. Unlike the two other diel cycles, the ^{222}Rn peak during intermediate tidal cycle 5 was delayed by two hours following the lowest water level period (Fig. 6). Consequently, most of the ^{222}Rn was accounted for the flood period. This delay potentially occurred for pCO_2 as well but did not seem to have happened for DIC or DOC (Fig. 6).

3.1.2. Porewater and sediment observations

The porewater concentrations were highly variable between sites and with depth. Overall, the median value used for the porewater end members for DIC, DOC, and ^{222}Rn were 4,861 ± 2,398 mmol m^{-3}, 219 ± 78.5 mmol m^{-3}, and 77,520 ± 41,660 dpm m^{-3}, respectively (Table 2). These values were 26.4, 3.8, and 1.8 folds higher than for median surface water concentration for radon, DIC, and DOC, respectively. The piezometers experiment at the transition *Avicennia*/mudflat revealed higher radon concentrations with depth with a maximum of 88,326 dpm m^{-3} at 150 cm but unclear trends for DOC (Table 2). The highest radon, DIC, and DOC concentrations in porewater were all reported in the mudflat, followed by the *Avicennia* and the *Rhizophora* stand. For instance, the maximum radon concentration was 164,160 dpm m^{-3} which about two fold higher than the highest value of in sediment under *Avicennia* (87,384 dpm m^{-3}) and *Rhizophora* vegetation (91,687 dpm m^{-3}). Similarly, DIC maximum concentrations in the mudflat were as high as 8,661 mmol m^{-3} and about 1.4–3.7 fold higher than in the *Avicennia* (6,240 mmol m^{-3}) and *Rhizophora* stands (2,347 mmol m^{-3}). Only DOC showed little variability with concentrations between 143 and 401 mmol m^{-3} between the four plots (Table 2).

Sediment between the three stands had some distinct characteristics with a sand particle size fraction > 9% under *Rhizophora* vegetation while only ~5.0% in the mudflat and 1.8% under the *Avicennia* vegetation (Table 2). The proportion of clay was similar between sites with a value close to 7.5%; and the silt fraction ranged from 72% in the *Rhizophora* stand to 90% under the *Avicennia*. The organic carbon content was on average 6.7 ± 0.7% in the 100 cm at the *Rhizophora* stand and 2.3 ± 0.2% and 2.4 ± 0.5% under *Avicennia* cover and in the mudflat, respectively.

3.2. Hydrodynamics

Contrasting water level variation, as a consequence of tides, induced contrasting flow velocity, water discharge and water exchange values (Fig. 7). An asymmetry between the ebb and flood flow velocities was observed, with the highest depth-averaged velocity being systematically recorded during the ebb tide, except for the intermediate tidal cycle 5 (Fig. 7). The maximum exchange (Q) during the flood period was 6,915 m^3 per 15 min (= 7.7 m^3 sec^{-1}), which was slightly higher than the maximum discharge for the ebb period of 6,150 m^3 per 15 min (= 6.8 m^3 sec^{-1}).

The water mass balance also had contrasting budgets, with the symmetric and intermediate 25-h diel cycles being net water importers ($Q_{flood} > Q_{ebb}$) and the asymmetric diel cycle being net exporters ($Q_{flood} < Q_{ebb}$; Fig. 7 fourth row).

3.3. Porewater discharge, mass balance budgets and carbon exchange

A radon mass balance model was developed for two symmetric tidal cycles, one asymmetric tidal cycle, and two intermediate tidal cycles. All five tidal cycles were selected to (i) have an ebb and flood tide; (ii) capture the low tide period; and (iii) present a balanced water budget ($Q_{flood} = Q_{ebb}$). Among the variables that were used for the development and correction of the ^{222}Rn mass balance, atmospheric evasion of ^{222}Rn accounted for 12% to 47% of the ^{222}Rn output (Table 3). Radium and radon decay were the smallest radon source and sink, respectively, during all the tidal cycles (Table 3). Porewater exchange varied from 3.1 ± 1.6 cm day^{-1} during the intermediate tidal cycle 4 to 7.1 ± 2.4 cm d^{-1} during the intermediate tidal cycle 5 (Fig. 8). When comparing porewater exchange during the ebb and flood tide, greater discharge was consistently reported during the ebb tide with the exception of intermediate tidal cycle 5, when porewater discharge at ebb tide was 1.0 ± 0.3 cm per tidal cycle and 1.3 ± 0.5 cm per tidal cycle during flood tide (Table 3).

All the tidal cycles were net DIC and DOC exporters, with exchanges ranging from 20.6 ± 1.9 mmolC m^{-2} day^{-1} to 67.7 ± 7.9 mmolC m^{-2} day^{-1} for DOC and from 352 ± 34 mmolC m^{-2} day^{-1} to

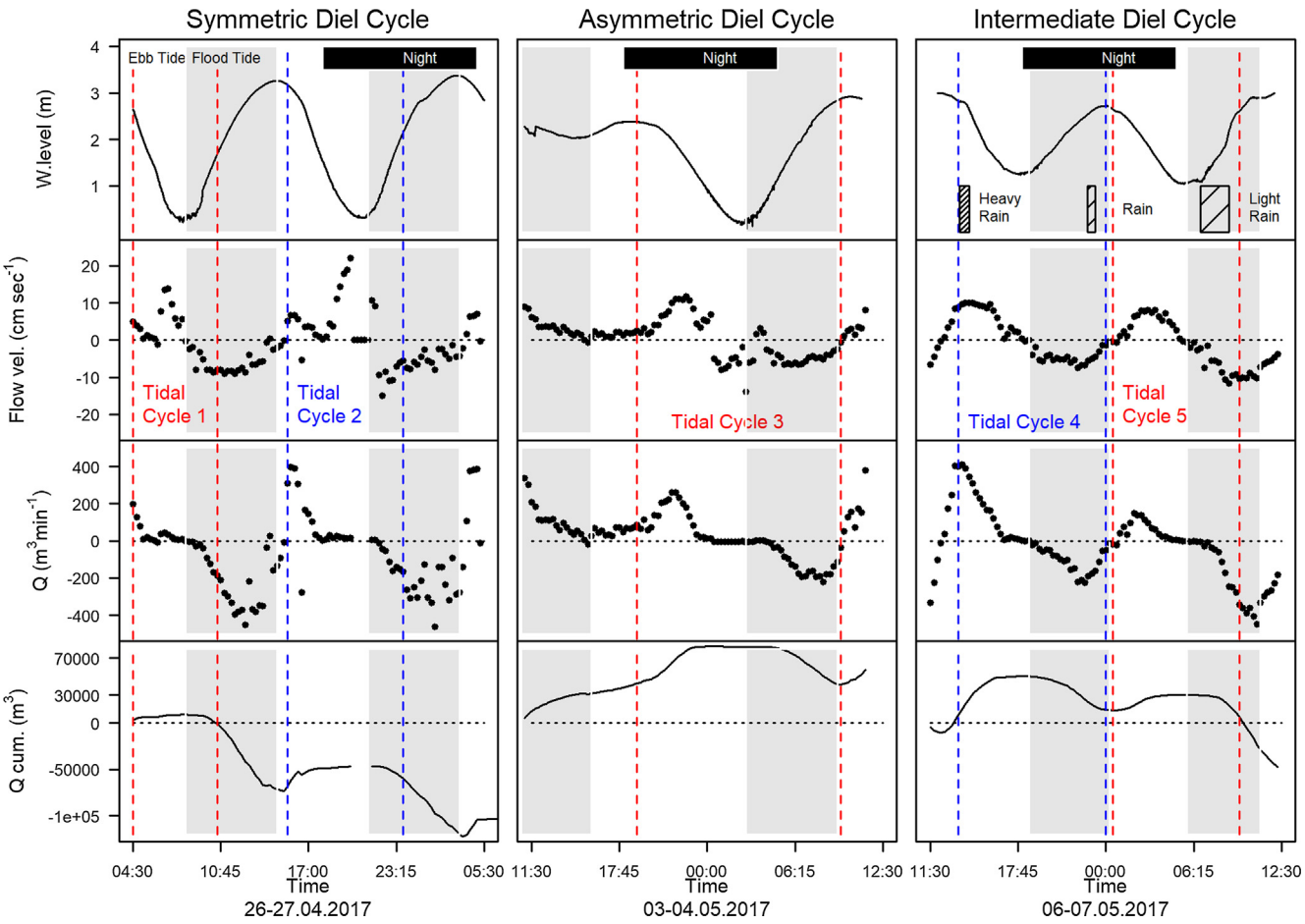

Fig. 7. Diel cycle (25-h) of hydrodynamic parameters in the Can Gio Mangrove tidal creek in April and May 2017. Flow velocities (second row), water discharge (Q; $m^3\ min^{-1}$; third row), and cumulative discharge (Q cum.; m^3) were measured from the cross-section at equal distance from the head and the mouth of the tidal creek. Values above 0 indicate a net export (outflow) of water from the creek, values below 0 indicates a net import of water (inflow) to the creek into the mangrove forest. The shading background (grey) indicates flood tide; no background (white) indicates ebb tide; the black banner at the top indicates night.

677.7 ± 79 mmolC m^{-2} day^{-1} for DIC (Fig. 8). The largest exports of both DOC and DIC occurred during the asymmetric tidal cycle 3. The porewater contribution for DOC exchange was limited to 3%–19%, with an average porewater exchange of 3.9 ± 1.2 mmolC m^{-2} day^{-1}. High quantities of DIC from porewater was exported: contributions ranged from 17% to 75%; and the mean net export was 169.2 ± 63.4 mmolC m^{-2} day^{-1} (Fig. 8). The highest porewater contribution was observed during the intermediate tidal cycle 5 as porewater exchange contributed to 19% and 75% of the total DOC and DIC exported, respectively. This observation can directly be related to the lag observed between the ^{222}Rn signal and the low-tide period (Fig. 6).

The tidal creek was a net source of CO_2 to the atmosphere throughout the study (Fig. 8). The mean calculated fluxes from the four equations was 141.6 ± 50.8 mmolC m^{-2} day^{-1}. Between tidal cycles, the highest CO_2 evasion was reported during the asymmetric tidal cycle 3 (200.7 ± 30.1 mmolC m^{-2} day^{-1}), which was also when the highest mean absolute current velocities (5.6 ± 0.4 cm sec^{-1}) and pCO_2 concentrations (4,957 ± 3,644 µatm) occurred (Figs. 6 and 7).

Overall, DIC export was consistently one order of magnitude higher than DOC and CO_2 evasion (Fig. 9). The greatest dissolved carbon exchange occurred during the asymmetric tidal cycle 3, with a net export of import of 674. ± 74.9 mmolC m^{-2} day^{-1} for DIC, 200.0 ± 30.1 mmolC m^{-2} day^{-1} for CO_2 evasion and 67.7 ± 7.9 mmolC m^{-2} day^{-1} for DOC export (Fig. 8), among which 7% for DOC to 32% (for DIC) originated from porewater seepage, as determined from the ^{222}Rn mass balance model (Fig. 8).

4. Discussion

4.1. The influence of hydrodynamics on porewater discharge and carbon dynamics

Our study revealed a porewater input of carbon to the tidal creek of contrasting magnitude between and within the three diel cycles. Although intuitive but never directly tested, we hypothesised that water level controls porewater discharge, with the height of the creek bank being the threshold reference elevation for the discharge to occur. Results from this study showed that porewater discharge occurred only during the lowest low tides (Fig. 6). Similarly, when no porewater discharge occurred, because the water level did not drop sufficiently, the following porewater discharge at low tide had a greater magnitude, as observed during the asymmetric diel cycle (Fig. 6). The absence of discharge during one tidal cycle extend the residence time of porewater and its interaction with the sediment which lead to higher solute concentrations (Smith et al., 2016). Overall, our carbon concentration ranges and tidal trends observed were similar to a number of prior studies on carbon dynamics and porewater discharge in mangrove tidal creeks (Bouillon et al., 2007; Call et al., 2015; Linto et al., 2014; Maher et al., 2013).

Besides the general observation that water level controls the porewater discharge and consequently the tidal creek carbon dynamics, the intermediate diel cycle provides evidence that the influence of water level is indeed more complex that it can appear if only looking at the two most contrasting diel cycles (symmetric and asymmetric). First, the

Table 3
Terms used in the ^{222}Rn, mass balance porewater flux calculations. Water and porewater exchange are the results of outflow-inflow. Values above 0 indicates a net export (outflow) of water from the creek, values below 0 indicates a net import of water (inflow) to the creek. Porewater discharge is the sum of abs(inflow) + abs(outflow).

Variable	Symmetric Tidal cycle 1		Symmetric Tidal cycle 2		Asymmetric Tidal cycle 3		Intermediate Tidal cycle 4		Intermediate Tidal cycle 5	
	Ebb (A)	Flood (B)	Ebb (A)	Flood (B)	Ebb (A)	Flood (B)	Ebb (A)	Flood (B)	Ebb (A)	Flood (B)
Water discharge (10^3 m^3 tidal $cycle^{-1}$)	8.9	7.2	26.1	24.8	41.3	41.0	35.3	35.3	15.0	14.7
Radon Source (Input)										
Radon diffusion (10^5 dpm tidal $cycle^{-1}$)	13 (± 6.4)	16 (± 8.6)	26.4 (± 11)	57.6 (32.1)	32 (± 10)	117 (± 57)	27.5 (± 17.2)	91.7 (± 51.4)	28.5 (± 9.5)	23.4 (± 11.8)
Radium decay (10^5 dpm tidal $cycle^{-1}$)	0.6 (± 0.1)	0.0 (± 0.0)	1.6 (± 0.3)	0.3 (± 0.1)	1,7 (± 0.3)	4.0 (± 0.8)	1.3 (± 0.3)	3.9 (± 0.8)	1.6 (± 0.3)	1.3 (0.3)
Radon Sink (Output)										
Radon outgoing (10^5 dpm tidal $cycle^{-1}$)	348.9 (± 125)	334.2 (± 162)	602.4 (± 237)	1,140 (± 563)	1,963 (± 252)	1,026 (± 400)	685.2 (± 389)	513.5 (± 259)	518.9 (± 122)	1,294 (± 585)
Radon evasion (10^5 dpm tidal $cycle^{-1}$)	105.6 (43)	51.0 (± 17)	139 (± 54)	164 (± 89)	286 (± 65)	292 (± 154)	163.8 (± 103)	70.0 (± 39)	153.1 (± 49.4)	324.9 (± 165.9)
Radon decay (10^5 dpm tidal $cycle^{-1}$)	29.1 (± 13)	1.9 (± 1)	60.8 (± 17)	25.4 (± 9)	105 (± 27.6)	79.9 (± 37.7)	41.0 (± 25.0)	77.2 (± 42.1)	80.9 (± 24.4)	174.4 (± 85.5)
Missing radon (10^5 dpm tidal $cycle^{-1}$)	469.8 (± 139)	371.1 (± 164)	774.2 (± 250)	1,246 (± 579)	2,321 (± 279)	1,272 (± 453)	861.2 (± 417)	565.1 (± 275)	722.7 (± 141)	1,769 (± 629)
Radon end member (dpm m^{-3})	73,959 (± 12,026)		73,959 (± 12,026)		74,712 (± 14,469)		74,556 (± 14,328)		74,556 (± 14,338)	
Upst. Max Flooded Area (10^3 m^2)	90.7 (± 18)	173.1 (± 35)	119 (± 24)	369 (± 73.7)	98.0 (± 20)	381.6 (± 76)	113.1 (± 22.6)	304.1 (± 60.8)	89.0 (± 17.8)	177 (35.4)
Porewater exchange (cm tidal $cycle^{-1}$)	0.7 (± 0.2)	0.3 (± 0.1)	0.9 (± 0.3)	0.5 (± 0.3)	3.2 (± 0.7)	0.4 (± 0.2)	1.0 (± 0.5)	0.2 (± 0.1)	1.0 (± 0.3)	1.3 (± 0.5)
Duration	4h00	2h00	6h00	3h15	6h30	8h00	4h30	5h30	4h00	8h00
Porewater exchange (cm day^{-1})	**4.0 (± 1.5)**		**3.5 (± 1.4)**		**6.0 (± 1.5)**		**3.1 (± 1.6)**		**7.1 (± 2.4)**	

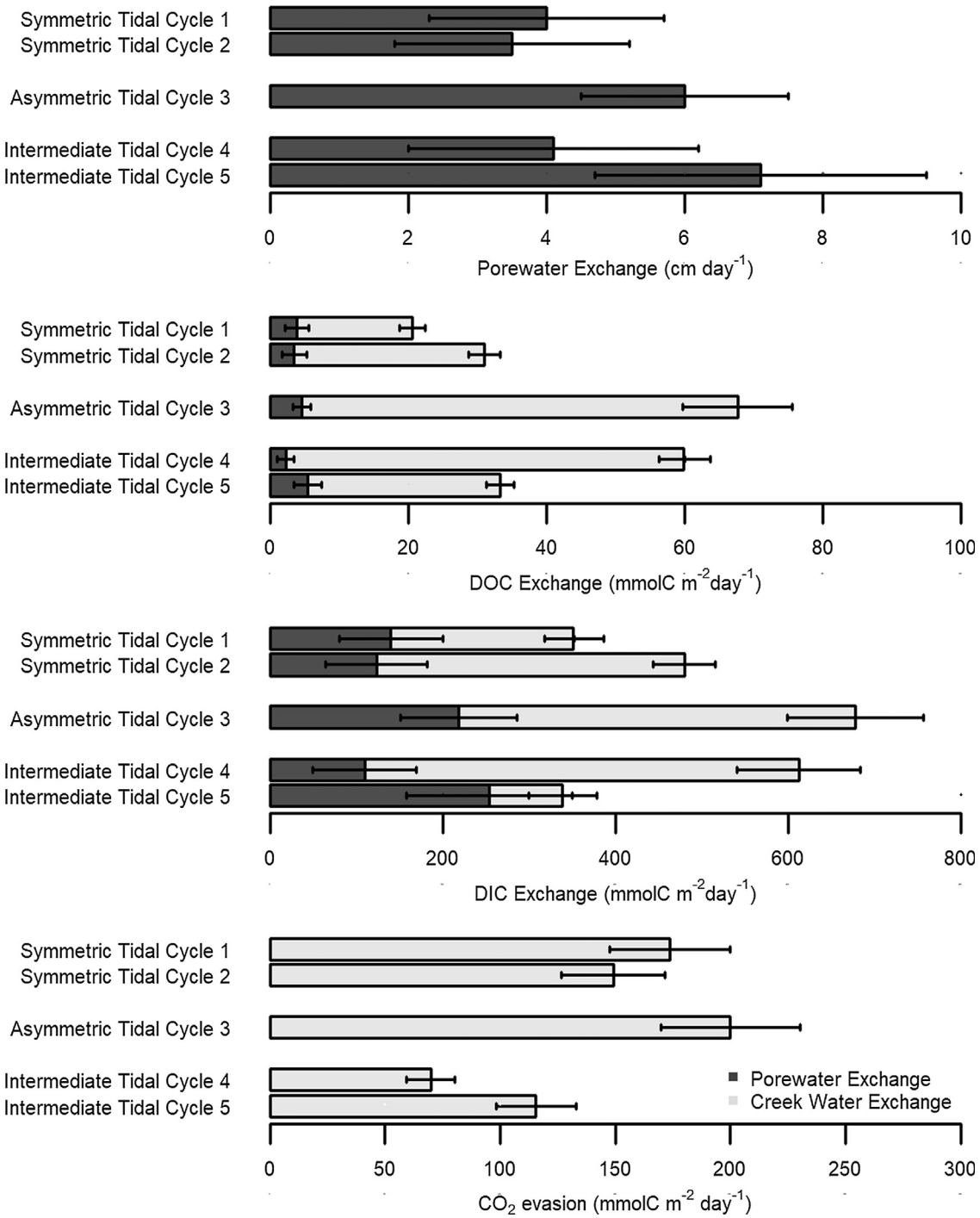

Fig. 8. Porewater exchange (cm d^{-1}), DIC exchange (mmolC m^{-2} day^{-1}), DOC exchange (mmolC m^{-2} day^{-1}), and CO_2 efflux (mmolC m^{-2} day^{-1}) during five tidal cycles in the Can Gio mangrove. The light grey bar-plot indicates the net water exchange, the dark grey bar-plot indicates the porewater exchange. All values suggest a net export from the tidal creek to coastal waters (DOC and DIC) and the atmosphere (CO_2 evasion).

DOC tidal trends and concentrations variability were not as clear as for DIC and pCO_2 during the intermediate diel cycle (Fig. 6). Three rain events occurred during this diel cycle. Considering that rainfall enhances water volume exchange, leaching of soluble organic matter and turbidity (Twilley, 1985), the steady DOC increase during this diel cycle might be explained by runoff and rain draining on the forest canopy to the surface creek water via throughfall and stemflow (typically $< 5\%$).

Second, a higher porewater discharge was observed during the intermediate tidal cycle 5 when compared to the intermediate tidal cycle 4, even though the water level difference was only 20 cm lower (Fig. 2), and the air-exposed creek bank period was only 25 min longer during the intermediate tidal cycle 5. Porewater navigates through the sediment via advection, following the hydrostatic gradient which leads to a discharge in the tidal creek during the ebb tide (Santos et al., 2012a). The lower the low tide, the steeper the gradient, and the greater the porewater discharge (Mazda and Ikeda, 2006), as observed during the symmetric diel cycle. Conversely, when water level remains high at low tide, the discharge is limited or absent, just as observed during the first low tide of the asymmetric diel cycle (Fig. 6). During the intermediate diel cycle, the lowest water level was 70 cm and 90 cm below the creek bank surface during the tidal cycle 4 and 5, respectively. This difference appeared to be sufficient to control the discharge process. Moreover,

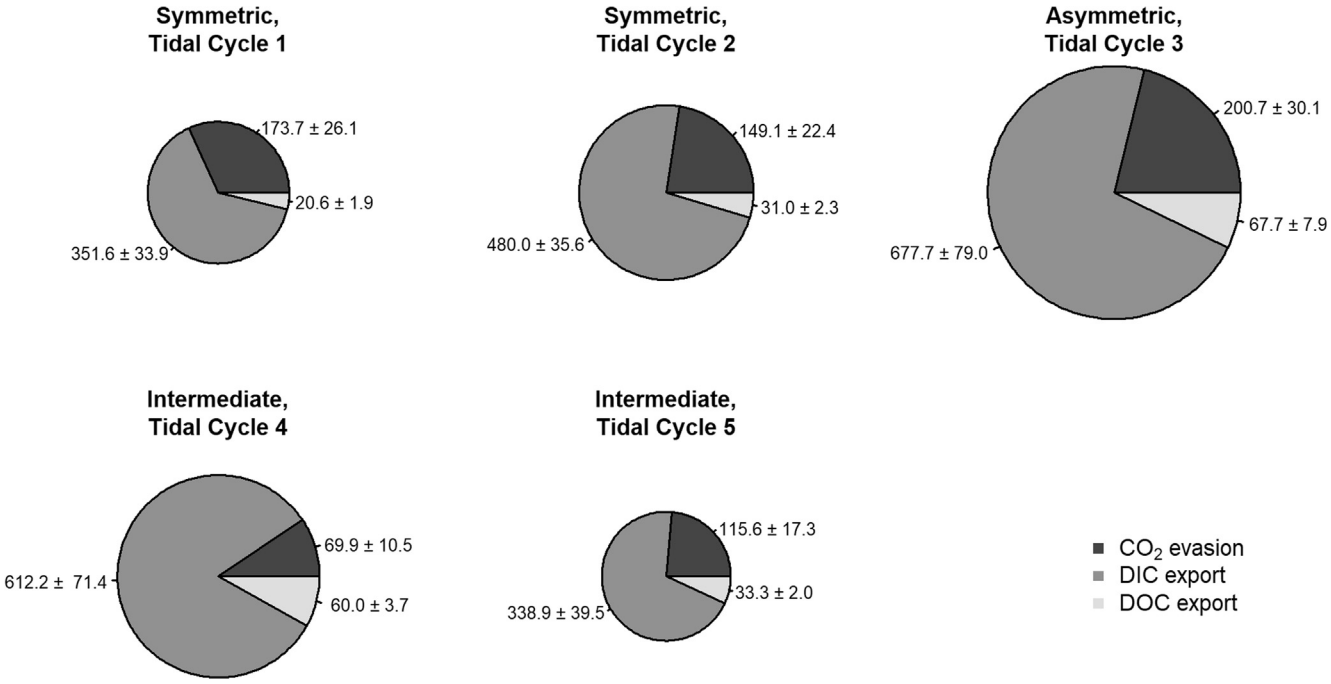

Fig. 9. Average portion of the carbon species /export from the tidal creek during the five different tidal cycles studied. Values are indicated in mmolC $m^{-2} d^{-1}$ (± STDEV).

this difference was amplified by the mechanism of discharge itself, as described above for the asymmetric diel cycle: a greater discharge follows a high low tide of no discharge (Smith et al., 2016).

A third observation from the intermediate diel cycle is the delay of about 2 h in porewater discharge during the tidal cycle 5, as indicated by the ^{222}Rn data (and possibly pCO_2; Fig. 6). No delay was reported during the other tidal cycles. This lag is likely because porewater continues to drain when the tidal flow shifts between slack and flood tides (Smith et al., 2016). As the water level did not drop too low (1.04 m), drainage out of the creek bank was not fully complete during ebb tide and continued during the early flood stage. Consequently, discharge peak was delayed when compared to the lowest water level period. Another condition for explaining this delay could be related to the physical influence of dense roots network. Kim and Hwang (2002) mentioned that a lag is common for groundwater discharge as the draining speed depends on the characteristics of the underlying rocks, sediments, and aquifers. In the mangrove system, draining speed most likely relies on sediment geometry/porosity and crab burrow density (Stieglitz et al., 2013). Below-ground root networks sediment, and particularly of *Avicennia* trees as they are present on the edge of the mangrove forest, may account for an additional obstacle in near-surface sediments by creating friction and slowing down the draining flow (Mazda et al., 2005). However, when the water level is lower than the roots layer of about 30 cm (Marchand et al., 2004), the friction is reduced and the discharge rate enhanced as observed during the symmetric and asymmetric diel cycles. Based on these observations, water level appears to control the magnitude, duration, and also the timing of porewater discharge.

4.2. Water, porewater, dic, and doc fluxes: In situ processes rather than tidal export

4.2.1. The importance of a mass balance approach in estimating material fluxes

The originality of this study lies in coupling synchronized high-frequency hydrodynamics, hydrogeochemical, and biogeochemical data together in mass balance models. Most prior studies calculated water exchange and material fluxes in tidal creeks using theoretical models, flumes or remote sensing data, all of which present approximate estimations rather than direct field measurements (Ayukai et al., 1998; Boto and Bunt, 1981; Romigh et al., 2006; Tait et al., 2016; Wattayakorn et al., 1990). Here, we estimated our mass balance model uncertainties following the basic rule of error propagation, which combines the analytical uncertainty of each term of the mass balances (Sadat-Noori et al., 2015). The main benefit of our experimental design is the low uncertainty estimation for water discharge (6%) as direct measurements were obtained for both, current velocity and the cross-section area. Analytical uncertainties for DOC exchange (12%) and DIC exchange (16%) were also relatively low, partly because only two variables of reasonably high accuracy were used for this mass balance calculation (i.e. water discharge and samples concentration every hour). The CO_2 evasion had an overall uncertainty of 22% as it is based on theoretical gas velocity determination (Rosentreter et al., 2016).

Radon mass balance had five different variables which all had uncertainties that propagated (Table 3). The ^{222}Rn porewater end member value is a key variable but also an important source of uncertainty in the mass balance model, because of the large sample spatial heterogeneity (Atkins et al., 2013; Sadat-Noori et al., 2015). We attempted to cover this heterogeneity by collecting triplicated samples in the different vegetation stand and mudflat (Table 2). However, the standard error for porewater end member was still about 18%. Thus, the overall uncertainty was 20% to 40% in the porewater discharge per tidal cycle (Table 3), which is satisfactory when compared to the other radon mass balance approaches (see Table 4 in Sadat-Noori et al., 2015).

4.2.2. Water exchange in the tidal creek

The three 25-h diel cycles were selected to cover tidal oscillation disparity in the creek (Fig. 2). Results indicated contrasting water budgets, with the symmetric diel cycle being a net importer ($Q_{ebb} < Q_{flood}$), the asymmetric a net exporter ($Q_{ebb} < Q_{flood}$) and the intermediate dial tidal cycle a nearly balanced system (see Fig. 7). Although not representative of the full lunar cycle, when the 3 diel cycles were summed together the tidal creek was a net importer of 93,218 m^3 ($Q_{ebb} > Q_{flood}$). Thus, the water budget was not balanced over the three diel cycles assessed.

Prior studies conducted in mangrove and salt-marsh tidal creeks

also reported a higher water import than export, particularly during the dry season (Boon, 1975; Michot et al., 2011; Twilley, 1985; Twilley and Chen, 1998). Evapotranspiration contributes to a natural imbalance of import versus export (Twilley and Chen, 1998). However, the contribution of evapotranspiration is considered secondary in the tidal creek water budget and cannot explain such an imbalance (Michot et al., 2011). As an illustration, if considering an evapotranspiration rate of 3 cm day^{-1} (Wolanski et al., 1980) and an average upstream flooded area of 79,959 m^2 for the symmetric diel cycle, evapotranspiration would have removed 2,398 m^3 day^{-1} while the total imbalance was 120.1 10^3 m^3 day^{-1}. Rather than evapotranspiration, the water budget imbalance over a small time-period (i.e. diel cycle) is more likely a consequence of intertidal storage. The storage capacity of shallow water tidal systems in its sediment is a key parameter, along with friction in the creek channels, for creating tidal distortion to encourage sediment deposition and coastal stability which support intertidal vegetation establishment (Speer et al., 1991). The intertidal storage capacity is fluctuating over the lunar tidal cycle and explain this apparent imbalance at the daily scale (Friedrichs and Aubrey, 1988). Thus, an exhaustive balanced water budget in tidal creeks would require continuous measurements over a period of at least 14 days (half-lunar tidal cycle). Considering the extensive amount of work this would entail, we identified for this study five tidal cycles representative of the tidal oscillation variability over a lunar cycle and adjusted the time period to present a balanced water budget to estimate the porewater and dissolved carbon exchange.

4.2.3. Porewater exchange in the tidal creek

The mean porewater exchange during this study was 4.9 ± 1.5 cm day ^{1} using the radon mass balance model (Fig. 8). Within the five tidal cycles, asymmetric tidal cycle 3 and intermediate tidal cycle 5 were the periods with the greatest exchange of 6.0 ± 1.6 cm day^{-1} and 7.1 ± 2.4 cm day^{-1}, respectively. As described above, surface water level below the creek bank height (i.e. 1.94 m) and the absence of clear porewater discharge during the preceding low tide during low tide (Fig. 6) can explain the occurrence of porewater discharge as the water residence time in the sediment is extended. These two tidal cycles also shared the common characteristic of having the lowest high tide water level (< 2.7 m) before the ebb tide (Fig. 2). Applying the hypothesis from Call et al (2015) to our system, we can justify the greatest porewater discharge during these two tidal cycles as a result of "older" porewater discharge previously infiltrated in higher intertidal areas during tidal cycle of maximum high tide (e.g. symmetric diel cycle; Fig. 2) which drained through the sediment towards the creek as the hydrostatic pressure decreased with decreasing tidal amplitude.

Porewater exchange from this study were lower than previously quantified rates in six different tidal creeks along the Australian coastlines which varied from 2.1 to 35.5 cm day^{-1} (Tait et al., 2016). Although results are normalized on an area basis and a daily rate, it is difficult to compare values between sites as site-specific conditions such as tidal geometry, tidal prism, crab burrow density, and tidal amplitude can directly influence the discharge rate. In their study, bulk density accounted to be the only variable to explain porewater discharge variability between the different study sites (Tait et al., 2016).

Based on our observation, we suggest that that tidal amplitude could be a key variable. Greater discharge appeared to happen during low low tide (e.g. asymmetric tidal cycle 3) as well after a low high tide to allow previous infiltrated water to flow through the sediment towards the tidal creek (e.g. intermediate tidal cycle 5).

4.2.4. Dissolved carbon exchange and porewater-derived contribution in the tidal creek

During the five tidal cycles assessed, net export of DOC and DIC to coastal waters and CO_2 losses to the atmosphere were reported from the mangrove tidal creek at Can Gio. As no prior studies have combined the exchange of DOC, DIC and the evasion of CO_2, this study provides a first tidal creek carbon exchange assessment. Most of the carbon exported was in the form of DIC, which accounted for 69.5% to 82.5% of the total dissolved carbon exchange (Fig. 9). The second largest output was CO_2 evasion with a contribution of 9.4% to 31.8%, while DOC export only accounted for 3.8% to 8.1% of the total carbon exchange. The measured carbon exchange proportions were close to those in the review of Bouillon et al. (2008), who reported 73% DIC, 17% CO_2 evasion, and 10% DOC.

The contribution of DOC from porewater discharge in this study was overall limited as it did not account for > 19%. Porewater discharge had, however, a direct influence on DIC export with a contribution as high as 74% during the intermediate tidal cycle 5 and no < 18% during intermediate tidal cycle 4 even no the porewater discharge was limited during the period (Fig. 7). We highlight that our mass balance approach account for "direct" porewater discharge and do not consider porewater-derived carbon that could be in the water column because of seawater recirculation over multiple tidal cycles. Thus, the contribution of mangrove-derived carbon in the water column could be higher than what is suggested by our approach. Other organic sources such as phytoplankton, epiphytic algae, benthic microalgae, fungi and various other estuarine organic material, ultimately degraded and mineralized, could explain the remaining fraction of carbon pool (Bouillon et al., 2002; Maher et al., 2013).

High DIC export rate originating from mangroves and much lower DOC export has previously been observed and is confirmed by our model. DIC exchange of −97–85 mmolC m^{-2} day^{-}and 183 to 341 mmolC m^{-2} day^{-1} has been reported by Sippo et al. (2016) and Maher et al. (2013), respectively. Our results showed higher but comparable rates, with daily DIC exchange ranging from 352 ± 34 to 678 ± 79 mmolC m^{-2} day^{-1} which is also in the high range of the global DIC export estimation of 254 ± 235 mmolC m^{-2} day^{-1} (Bouillon et al., 2008). The prior measured DOC exchange was between 24.9 and 49.7 mmolC m^{-2} day^{-1} (Maher et al., 2013; Sippo et al., 2017). Here, values between the tidal cycles varied from 20.6 ± 1.9 to 67.7 ± 7.9 mmolC m^{-2} day^{-1} which is still similar to the global DOC export estimation of 41.6 ± 33.3 mmolC m^{-2} day^{-1} (Bouillon et al., 2008). The CO_2 evasion rates in this study were estimated at 69.9 ± 10.5 to 200 ± 30.0 mmolC m^{-2} day^{-1} which is, once again, higher than the global estimate of 56.5 mmolC m^{-2} day^{-1} (Rosentreter et al., 2018).

Although our results suggest that the export of carbon from the Can Gio mangrove forests is higher than average global estimates, we only provided data in the very same tidal creek and during the dry season. Moreover, our measurements were conducted at equal distance from the head and the mouth of the tidal creek while previous studies chose their sampling location at the creek mouth. Measuring carbon fluxes within the tidal creek minimizes the losses associated to creek water transport such as respiration, photo-mineralization, or flocculation for DOC and evasion for DIC and CO_2 (Borges et al., 2003; Dittmar et al., 2006). Thus, this mid-creek location is probably more representative of the whole tidal creek dynamics as it integrates the loss of CO_2 when water is transiting within the tidal creek (Call et al., 2015; Leopold et al., 2017).

Another explanation for the greater carbon export estimates is the location of the study site at a low latitude. The Can Gio Mangrove Biosphere Reserve is representative of highly productive mangroves of the Asia-Pacific region with an average mature-stand ecosystem carbon stock of 910.7 ± 32.2 Mg C ha^{-1}, including 667.4 ± 11.8 MgC ha^{-1} (73%) in the sediments (Dung et al., 2016). This high carbon stock is expected to be partially decomposed and exported via tidal action as well as rapidly mineralized because of high temperatures and humidity rates in the region that support bacterial activity (Bouillon et al., 2003; Kristensen and Suraswadi, 2002).

Further, previous studies have reported significant seasonal variation in tidal creeks hydrodynamics, with an overall relation between

high precipitation and net carbon export. Higher dissolved and particulate carbon concentrations during the wet season are expected because rainfall increases the load of particulate and soluble organic carbon via throughfall and stemflow (Twilley, 1985). Moreover, a decrease in salinity is expected. All those processes have been identified to stimulate biological productivity (either vegetation, benthic or pelagic), and thus enhance the organic and inorganic carbon dynamics (Koné and Borges, 2008; Linto et al., 2014). Hence, to get a complete estimation of the carbon export from tidal creek it is important to quantify exchange during the dry and wet season (or monthly).

5. Conclusions

We conducted multiple continuous measurements and used a mass balance approach to estimate the volume of water, porewater and dissolved carbon (both organic and inorganic) imported and exported from a mangrove tidal creek. This work was directly related to testing the historical outwelling hypothesis and the tidal carbon export hypothesis. We identified the direct contribution of porewater discharge to tidal creek carbon dynamics, particularly intense during the lowest low tides. A net export of DOC and DIC, as well as a net CO_2 loss to the atmosphere, was found during the five tidal cycles assessed. On average, DIC accounted for 72% of the total carbon output, CO_2 evasion for 22%, and DOC for 6%. The contribution of porewater discharge in the dissolved inorganic carbon export was estimated at 38%. Porewater discharge was suggested to increase during tidal cycles of low-low tide or low–high tide as it changed the hydrostatic pressure and facilitated porewater seepage. Overall, our results were in the high range of previous estimates of dissolved carbon export with an average DIC, DOC export and CO2 evasion of 492 ± 52 ,42 ± 4, and 142 ± 21 mmolC m^{-2} day^{-1}, respectively.

The export of material from mangroves to coastal waters, and particularly carbon, is a recurrent research hypothesis that has led to many speculations and simplifications. The combination of decades of research advancement and the association of multiple automated quasi-continuous equipment might help constrain this process and clearly determine the fate of dissolved carbon from mangrove tidal creeks. Considering the dynamic state of mangrove tidal creeks, high definition and high frequency direct measurements, as presented in this study, need to be conducted over full lunar tidal cycles, over contrasting seasons, at different locations within the tidal creek (head, midway, and mouth) and between mangroves of different tidal amplitudes to provide accurate estimations of carbon fluxes with the broader coastal zone.

Conflict of interest

The authors declare no conflict of interest.

Acknowledgements

The authors thank Truong Phat, Le Thi Dien and Captain Quang for their assistance in the field, students from University of Science Vietnam National University and the NUS Mangrove Lab for logistics assistance, Winston Chow (National University of Singapore) for the loan of the Kestrel equipment, Émilie Strady (Institut de Recherche pour le Développement) for laboratory space, Jean Pierre Lefebvre (Institut de Recherche pour le Développement) for critical comments on hydrodynamics, Erik Horstman (University of Waikato) for the discussion regarding the hydrodynamic measurement set-up, Bas Borsje and Suzanne Hulscher (University of Twente), Tjeerd Bouma and Lennart van IJzerloo (Royal Netherlands Institute for Sea Research) for arranging the use of measurement equipment, Janie Masse Dufresne (Polytechnique Montreal) for assistance with laboratory work, Ana Maria Escobar Cardenas for the help related to the graphical work presented in this paper. . This project was supported by a Singapore Ministry of Education's AcRF Tier 1 grant (FY2014-FRC4-003; WBS-R-109-000-192-112) and the Air Liquide Foundation. PW was supported by the research programme BE SAFE, financed primarily by the Netherlands Organization for Scientific Research (NWO; 850.13.012).

References

Abril, G., Commarieu, M.-V., Sottolichio, A., Bretel, P., Guerin, F., 2009. Turbidity limits gas exchange in a large macrotidal estuary. Estuar. Coast. Shelf Sci. 83, 342–348.
Alongi, D.M., 2014. Carbon cycling and storage in mangrove forests. Ann. Rev. Mar. Sci. 6, 195–219.
Amorocho, J., DeVries, J., 1980. A new evaluation of the wind stress coefficient over water surfaces. J. Geophys. Res. Oceans 85, 433–442.
Atkins, M.L., Santos, I.R., Ruiz-Halpern, S., Maher, D.T., 2013. Carbon dioxide dynamics driven by groundwater discharge in a coastal floodplain creek. J. Hydrol. 493, 30–42.
Ayukai, T., Miller, D., Wolanski, E., Spagnol, S., 1998. Fluxes of nutrients and dissolved and particulate organic carbon in two mangrove creeks in northeastern Australia. Mangrov. Salt Marsh. 2, 223–230.
Baudron, P., Cockenpot, S., Lopez-Castejon, F., Radakovitch, O., Gilabert, J., Mayer, A., et al., 2015. Combining radon, short-lived radium isotopes and hydrodynamic modeling to assess submarine groundwater discharge from an anthropized semiarid watershed to a Mediterranean lagoon (Mar Menor, SE Spain). J. Hydrol. 525, 55–71.
Boon, J.D., 1975. Tidal discharge asymmetry in a salt marsh drainage system. Limnol. Oceanogr. 20, 71–80.
Borges, A., Abril, G., 2011. 5.04-Carbon dioxide and methane dynamics in estuaries. Treatise on Estuarine and Coastal Science. Biogeochemistry 119–161.
Borges, A.V., Djenidi, S., Lacroix, G., Theate, J., Delille, B., Frankignoulle, M., 2003. Atmospheric CO2 flux from mangrove surrounding waters. Geophys. Res. Lett. 30.
Boto, K.G., Bunt, J.S., 1981. Tidal export of particulate organic matter from a northern Australian mangrove system. Estuar. Coast. Shelf Sci. 13, 247–255.
Boto, K.G., Wellington, J.T., 1988. Seasonal variations in concentrations and fluxes of dissolved organic and inorganic materials in a tropical, tidally-dominated, mangrove waterway. Mar. Ecol. Prog. Ser. 151–160.
S. Bouillon A.V. Borges E. Castañeda-Moya K. Diele T. Dittmar N.C. Duke et al. Mangrove production and carbon sinks: a revision of global budget estimates Global Biogeochem. Cycles 2008 22 GB2013.
Bouillon, S., Koedam, N., Raman, A.V., Dehairs, F., 2002. Primary producers sustaining macro-invertebrate communities in intertidal mangrove forests. Oecologia 130, 441–448.
Bouillon, S., Frankignoulle, M., Dehairs, F., Velimirov, B., Eiler, A., Abril, G., et al., 2003. Inorganic and organic carbon biogeochemistry in the Gautami Godavari estuary (Andhra Pradesh, India) during pre-monsoon: The local impact of extensive mangrove forests. Global Biogeochem. Cycles 17.
Bouillon, S., Middelburg, J.J., Dehairs, F., Borges, A.V., Abril, G., Flindt, M.R., et al., 2007. Importance of intertidal sediment processes and porewater exchange on the water column biogeochemistry in a pristine mangrove creek (Ras Dege, Tanzania). Biogeosciences 4, 311–322.
Burnett, W.C., Dulaiova, H., 2003. Estimating the dynamics of groundwater input into the coastal zone via continuous radon-222 measurements. J. Environ. Radioactiv. 69, 21–35.
Burnett, W.C., Taniguchi, M., Oberdorfer, J., 2001. Measurement and significance of the direct discharge of groundwater into the coastal zone. J. Sea Res. 46, 109–116.
Call, M., Maher, D., Santos, I., Ruiz-Halpern, S., Mangion, P., Sanders, C., et al., 2015. Spatial and temporal variability of carbon dioxide and methane fluxes over semi-diurnal and spring–neap–spring timescales in a mangrove creek. Geochim. Cosmochim. Acta 150, 211–225.
Conley, D.C., 2015. Drivers: Waves and Tides. Coastal Environments and Global Change. John Wiley & Sons, Ltd., pp. 79–103.
Dickson, A., Millero, F.J., 1987. A comparison of the equilibrium constants for the dissociation of carbonic acid in seawater media. Deep Sea Res. Part A 34, 1733–1743.
Dittmar, T., Hertkorn, N., Kattner, G., Lara, R.J., 2006. Mangroves, a major source of dissolved organic carbon to the oceans. Global Biogeochem. Cycles 20.
Dittmar, T., Koch, B., Jaffé, R., 2009. Tools for studying biogeochemical connectivity among tropical coastal ecosystems. Ecological Connectivity among Tropical Coastal Ecosystems. Springer pp. 425–455.
Dittmar, T., Lara, R.J., 2001. Do mangroves rather than rivers provide nutrients to coastal environments south of the Amazon River? Evidence from long-term flux measurements. Mar. Ecol. Prog. Ser. 213, 67–77.
Dulaiova, H., Gonneea, M.E., Henderson, P.B., Charette, M.A., 2008. Geochemical and physical sources of radon variation in a subterranean estuary—implications for groundwater radon activities in submarine groundwater discharge studies. Mar. Chem. 110, 120–127.
Dung, L.V., Tue, N.T., Nhuan, M.T., Omori, K., 2016. Carbon storage in a restored mangrove forest in Can Gio Mangrove Forest Park, Mekong Delta, Vietnam. Forest Ecol. Manage. 380, 31–40.
Fagherazzi, S., Wiberg, P.L., Temmerman, S., Struyf, E., Zhao, Y., Raymond, P.A., 2013. Fluxes of water, sediments, and biogeochemical compounds in salt marshes. Ecol. Process. 2, 3.
Friedrichs, C.T., Aubrey, D.G., 1988. Non-linear tidal distortion in shallow well-mixed estuaries: a synthesis. Estuar. Coast. Shelf Sci. 27, 521–545.
Gleeson, J., Santos, I.R., Maher, D.T., Golsby-Smith, L., 2013. Groundwater-surface water exchange in a mangrove tidal creek: Evidence from natural geochemical tracers and implications for nutrient budgets. Mar. Chem. 156, 27–37.
Gran, G., 1952. Determination of the equivalence point in potentiometric titrations. Part II. Analyst 77, 661–671.

Ho, D.T., Coffineau, N., Hickman, B., Chow, N., Koffman, T., Schlosser, P., 2016. Influence of current velocity and wind speed on air-water gas exchange in a mangrove estuary. Geophys. Res. Lett.
Ho, D.T., Ferron, S., Engel, V.C., Larsen, L.G., Barr, J.G., 2014. Air- water gas exchange and CO_2 flux in a mangrove- dominated estuary. Geophys. Res. Lett. 41, 108–113.
Holloway, C.J., Santos, I.R., Tait, D.R., Sanders, C.J., Rose, A.L., Schnetger, B., et al., 2016. Manganese and iron release from mangrove porewaters: a significant component of oceanic budgets? Mar. Chem. 184, 43–52.
Horstman, E., Balke, T., Bouma, T., Dohmen-Janssen, M., Hulscher, S., 2011. Optimizing methods to measure hydrodynamics in coastal wetlands: evaluating the use and positioning of ADV, ADCP AND HR-ADCP. Coast. Eng. Proceed. 1, 51.
Horstman, E.M., Dohmen-Janssen, C.M., Hulscher, S.J., 2013. Flow routing in mangrove forests: A field study in Trang province, Thailand. Cont. Shelf Res. 71, 52–67.
Kearney, W.S., Mariotti, G., Deegan, L.A., Fagherazzi, S., 2017. Stage-discharge relationship in tidal channels. Limnol. Oceanogr. Methods 15, 394–407.
Kim, G., Hwang, D.W., 2002. Tidal pumping of groundwater into the coastal ocean revealed from submarine ^{222}Rn and CH_4 monitoring. Geophys. Res. Lett. 29.
Koné, Y.J.M., Borges, A., 2008. Dissolved inorganic carbon dynamics in the waters surrounding forested mangroves of the Ca Mau Province (Vietnam). Estuarine. Coastal and Shelf Science 77, 409–421.
Kristensen, E., Suraswadi, P., 2002. Carbon, nitrogen and phosphorus dynamics in creek water of a southeast Asian mangrove forest. Hydrobiologia 474, 197–211.
Lee, S., 1995. Mangrove outwelling: a review. Hydrobiologia 295, 203–212.
Leopold, A., Marchand, C., Deborde, J., Allenbach, M., 2017. Water Biogeochemistry of a Mangrove-Dominated Estuary Under a Semi-Arid Climate (New Caledonia). Estuaries Coasts 40, 773–791.
Lewis E, Wallace D, Allison LJ. Program developed for CO2 system calculations: Carbon Dioxide Information Analysis Center, managed by Lockheed Martin Energy Research Corporation for the US Department of Energy Tennessee, 1998.
Linto, N., Barnes, J., Ramachandran, R., Divia, J., Ramachandran, P., Upstill-Goddard, R.C., 2014. Carbon Dioxide and Methane Emissions from Mangrove-Associated Waters of the Andaman Islands, Bay of Bengal. Estuaries Coasts 37, 381–398.
Macreadie, P.I., Serrano, O., Maher, D.T., Duarte, C.M., Beardall, J., 2017. Addressing calcium carbonate cycling in blue carbon accounting. Limnol. Oceanogr. Lett.
Maher, D.T., Santos, I.R., Golsby-Smith, L., Gleeson, J., Eyre, B.D., 2013. Groundwater-derived dissolved inorganic and organic carbon exports from a mangrove tidal creek: The missing mangrove carbon sink? Limnol. Oceanogr. 58, 475–488.
Marchand, C., Baltzer, F., Lallier-Verges, E., Alberic, P., 2004. Pore-water chemistry in mangrove sediments: relationship with species composition and developmental stages (French Guiana). Mar. Geol. 208, 361–381.
Martens, C.S., Klump, J., Kipphut, G., 1980. Sediment-water chemical exchange in the coastal zone traced by in situ radon-222 flux measurements. Science 208, 285–288.
Mazda, Y., Ikeda, Y., 2006. Behavior of the groundwater in a riverine-type mangrove forest. Wetlands Ecol. Manage. 14, 477–488.
Mazda, Y., Kobashi, D., Okada, S., 2005. Tidal-scale hydrodynamics within mangrove swamps. Wetlands Ecol. Manage. 13, 647–655.
Mazda, Y., Magi, M., Nanao, H., Kogo, M., Miyagi, T., Kanazawa, N., et al., 2002. Coastal erosion due to long-term human impact on mangrove forests. Wetlands Ecol. Manage. 10, 1–9.
Mehrbach C. Measurement of the apparent dissociation constants of carbonic acid in seawater at atmospheric pressure, 1973.
Michot, B., Meselhe, E.A., Rivera-Monroy, V.H., Coronado-Molina, C., Twilley, R.R., 2011. A tidal creek water budget: estimation of groundwater discharge and overland flow using hydrologic modeling in the Southern Everglades. Estuar. Coast. Shelf Sci. 93, 438–448.
Nixon, S.W. 1980. Between coastal marshes and coastal waters—a review of twenty years of speculation and research on the role of salt marshes in estuarine productivity and water chemistry. Estuarine and wetland processes. Springer, pp. 437–525.
Nuttle, W.K., Harvey, J.W., 1995. Fluxes of water and solute in a coastal wetland sediment. l. The contribution of regional groundwater discharge. J. Hydrol. 164, 89–107.
Odum EP. A research challenge: evaluating the productivity of coastal and estuarine water. in: Proceedings of the 2nd Sea Grant conference. Graduate School of Oceanography, University of Rhode Island, 1968, pp. 63–64.
Odum EP. Tidal marshes as outwelling/pulsing systems. Concepts and controversies in tidal marsh ecology. Springer, 2002, pp. 3–7.
Peng, T.H., Takahashi, T., Broecker, W., 1974. Surface radon measurements in the North Pacific Ocean station PAPA. J. Geophys. Res. 79, 1772–1780.
Peterson, R.N., Santos, I.R., Burnett, W.C., 2010. Evaluating groundwater discharge to tidal rivers based on a Rn-222 time-series approach. Estuari. Coastal and Shelf Science 86, 165–178.
Romigh, M.M., Davis, S.E., Rivera-Monroy, V.H., Twilley, R.R., 2006. Flux of organic carbon in a riverine mangrove wetland in the Florida Coastal Everglades. Hydrobiologia 569, 505–516.
Rosentreter, J., Maher, D., Ho, D., Call, M., Barr, J., Eyre, B., 2016. Spatial and temporal variability of CO_2 and CH_4 gas transfer velocities and quantification of the CH_4 microbubble flux in mangrove dominated estuaries. Limnol. Oceanogr.
Rosentreter, J.A., Maher, D., Erler, D., Murray, R., Eyre, B., 2018. Seasonal and temporal CO_2 dynamics in three tropical mangrove creeks–A revision of global mangrove CO_2 emissions. Geochim. Cosmochim. Acta 222, 729–745.
Sadat-Noori, M., Maher, D.T., Santos, I.R., 2016. Groundwater discharge as a source of dissolved carbon and greenhouse gases in a subtropical estuary. Estuaries Coasts 39, 639–656.
Sadat-Noori, M., Santos, I.R., Sanders, C.J., Sanders, L.M., Maher, D.T., 2015. Groundwater discharge into an estuary using spatially distributed radon time series and radium isotopes. J. Hydrol. 528, 703–719.
Sánchez-Carrillo, S., Sánchez-Andrés, R., Alatorre, L.C., Angeler, D., Álvarez-Cobelas, M., Arreola-Lizárraga, J., 2009. Nutrient fluxes in a semi-arid microtidal mangrove wetland in the Gulf of California. Estuarine. Coast. Shelf Sci. 82, 654–662.
Santos, I.R., Eyre, B.D., Huettel, M., 2012a. The driving forces of porewater and groundwater flow in permeable coastal sediments: a review. Estuar. Coast. Shelf Sci. 98, 1–15.
Santos, I.R., Maher, D.T., Eyre, B.D., 2012b. Coupling automated radon and carbon dioxide measurements in coastal waters. Environ. Sci. Technol. 46, 7685–7691.
Sippo, J.Z., Maher, D.T., Tait, D.R., Holloway, C., Santos, I.R., 2016. Are mangroves drivers or buffers of coastal acidification? Insights from alkalinity and dissolved inorganic carbon export estimates across a latitudinal transect. Global Biogeochem. Cycles 30, 753–766.
Sippo, J.Z., Maher, D.T., Tait, D.R., Ruiz-Halpern, S., Sanders, C.J., Santos, I.R., 2017. Mangrove outwelling is a significant source of oceanic exchangeable organic carbon. Limnol. Oceanogr. Lett. 2, 1–8.
Smith, C.G., Price, R.M., Swarzenski, P.W., Stalker, J.C., 2016. The role of ocean tides on groundwater-surface water exchange in a mangrove-dominated Estuary: Shark River Slough, Florida Coastal Everglades, USA. Estuaries Coasts 39, 1600–1616.
Smith, S.V., 2013. Parsing the oceanic calcium carbonate cycle: a net atmospheric carbon dioxide source or a sink? Assoc. Sci. Limnol. Oceanogr.
SonTek. 1997. Sontek ADVField acoustic Doppler velocimeter: technical documentation. version 4.0. San Diego, CA: SanTek.
Sousa W, Dangremond E. 6.04 Trophic Interactions in Coastal and Estuarine Mangrove Forest Ecosystems. 2011.
Stieglitz, T.C., Clark, J.F., Hancock, G.J., 2013. The mangrove pump: The tidal flushing of animal burrows in a tropical mangrove forest determined from radionuclide budgets. Geochim. Cosmochim. Acta 102, 12–22.
Sugimura, Y., Suzuki, Y., 1988. A high-temperature catalytic oxidation method for the determination of non-volatile dissolved organic carbon in seawater by direct injection of a liquid sample. Mar. Chem. 24, 105–131.
Speer, P.E., Aubrey, D.G., Friedrichs, C.T., 1991. Nonlinear hydrodynamics of shallow tidal inlet/bay systems. Tidal Hydrodynam. 321–339.
Tait, D.R., Maher, D.T., Macklin, P.A., Santos, I.R., 2016. Mangrove pore water exchange across a latitudinal gradient. Geophys. Res. Lett. 43, 3334–3341.
Twilley, R.R., 1985. The exchange of organic carbon in basin mangrove forests in a southwest Florida estuary. Estuar. Coast. Shelf Sci. 20, 543–557.
Twilley, R.R., Chen, R., 1998. A water budget and hydrology model of a basin mangrove forest in Rookery Bay, Florida. Mar. Freshw. Res. 49, 309–323.
Twilley, R.R., Rivera-Monroy, V.H., 2009. Ecogeomorphic models of nutrient biogeochemistry for mangrove wetlands. Coastal wetlands: an integrated ecosystem approach. Elsevier, Amsterdam, pp. 641–683.
Ullman, W.J., Aller, R.C., 1982. Diffusion coefficients in nearshore marine sediments. Limnol. Oceanogr. 27, 552–556.
UNFCCC C. Adoption of the Paris Agreement. I: Proposal by the President (Draft Decision), United Nations Office, Geneva (Switzerland) 2015.
Wanninkhof, R., 1992. Relationship between wind speed and gas exchange over the ocean. J. Geophys. Res. Oceans 97, 7373–7382.
Wanninkhof, R., 2014. Relationship between wind speed and gas exchange over the ocean revisited. Limnol. Oceanogr. Methods 12, 351–362.
Wanninkhof, R., Asher, W.E., Ho, D.T., Sweeney, C., McGillis, W.R., 2009. Advances in quantifying air-sea gas exchange and environmental forcing. Ann. Rev. Mar. Sci.
Wattayakorn, G., Wolanski, E., Kjerfve, B., 1990. Mixing, trapping and outwelling in the Klong Ngao mangrove swamp, Thailand. Estuar. Coast. Shelf Sci. 31, 667–688.
Weiss, R.F., 1974. Carbon dioxide in water and seawater: the solubility of a non-ideal gas. Mar. Chem. 2, 203–215.
Willemsen, P.W.J.M., Horstman, E., Borsje, B.W., Friess, D., Dohmen-Janssen, C.M., 2016. Sensitivity of the sediment trapping capacity of an estuarine mangrove forest. Geomorphology 273, 189–201.
Wolanski, E., Jones, M., Bunt, J., 1980. Hydrodynamics of a tidal creek-mangrove swamp system. Mar. Freshw. Res. 31, 431–450.
Wolanski, E., Mazda, Y., Ridd, P., 1993. Mangrove hydrodynamics. Trop. Mangrove Ecosyst. 43–62.
Woodroffe, C., 1992. Mangrove sediments and geomorphology. Trop. Mangrove Ecosyst. 7–41.
World Bank, 2017. Climate Change Knowledge Portal. accessed 22.12.17. http://sdwebx.worldbank.org/climateportal/index.cfm?page=downscaled_data_download&menu=historical.